Accepted Manuscript

Journal of the Geological Society

Fault motion reversals predating the Mw 6.3 2009 L'Aquila earthquake: Insights from synthetic aperture radar data

Stefano Mazzoli, Sergio Nardò, Alessandra Ascione, Valentino Di Donato, Carlo Terranova & Giuseppe Vilardo

DOI: https://doi.org/10.1144/jgs2020-016

To access the most recent version of this article, please click the DOI URL in the line above. When citing this article please include the above DOI.

Received 31 January 2020
Revised 16 January 2021
Accepted 1 February 2021

Supplementary material at https://doi.org/10.6084/m9.figshare.c.5289357

Fault motion reversals predating the Mw 6.3 2009 L'Aquila earthquake: Insights from synthetic aperture radar data

Stefano Mazzoli[1], Sergio Nardò[2], Alessandra Ascione[2*], Valentino Di Donato[2], Carlo Terranova[3] Giuseppe Vilardo[4]

[1] School of Science and Technology, Geology Division, University of Camerino (MC), Italy

[2] Department of Earth, Environmental and Resources Sciences (DiSTAR), University of Naples Federico II, Italy

[3] Coordinator and Scientific Responsible of the Geoportale Nazionale INSPIRE - Unità di Assistenza Tecnica SOGESID S.p.A, at Ministero dell'Ambiente della Tutela del Territorio e del Mare (MATTM), Rome, Italy

[4] Istituto Nazionale di Geofisica e Vulcanologia (INGV), Sezione Osservatorio Vesuviano, Naples, Italy

* Correspondence: alessandra.ascione@unina.it

Abstract: The millimetre accuracy of Synthetic Aperture Radar (SAR) measurements and related multi-temporal data analyses provide fundamental information on surface displacements caused by strong earthquakes. The multi-temporal analysis of SAR interferometry (InSAR) data allows for the geometry, kinematics and temporal behaviour of earthquake-generating faults to be better constrained, and is being acknowledged as a promising technique in the field of earthquake precursors. We used SAR data obtained by multi-temporal interferometric techniques such as Permanent Scatterers Interferometry for the investigation of pre- to post-seismic ground displacements in the region struck by the Mw 6.3, 2009 L'Aquila earthquake. We analysed ERS and Envisat PS-datasets from ascending

and descending orbits, and COSMO-SkyMed PS-datasets from descending orbit, collectively covering a > 20-year long time span. On a yearly scale, a reversal of motions that affected the hanging-wall and footwall blocks of the earthquake-generating fault is detected. In particular, the hanging-wall block is characterized by preseismic uplift – that we document as being independent of any hydrological control – and eastward horizontal motion for about 6 years, followed by subsidence and westward motion (starting 8-6 months prior to the earthquake). We suggest that such a ground displacement pattern may represent an earthquake precursor signal.

The 2009 L'Aquila earthquakes (Chiarabba et al., 2009; Valoroso et al., 2013) have been among the strongest and more destructive seismic sequences that struck the Apennines of Italy in the last decades. They form part of a series of earthquakes that ruptured the NW-SE striking active normal fault system of central Italy between 1997 and 2016 (Fig. 1), in an interior part of the Apennines characterized by a regional interseismic NE-SW extension at a background rate of ~3 mm yr^{-1} (D'Agostino et al., 2011). The Mw 6.3, 2009 L'Aquila main shock was preceded by foreshocks that started in October 2008 (Di Luccio et al., 2010). Numerous aftershocks were also recorded (with more than 46,000 relocated events; Chiaraluce et al., 2011; Valoroso et al., 2013), including two strong events with Mw 5.4 and Mw 5.6 (Di Luccio et al., 2010; Valoroso et al., 2013). The main shock nucleated at a depth of 8.27 km and ruptured an 18 km long fault dipping 55°-60° to the SW (Chiarabba et al., 2009; Cirella et al., 2009; Pondrelli et al., 2010; Scognamiglio et al., 2010; Valoroso et al., 2013). The aftershock sequence (Valoroso et al., 2013) and the afterslip distribution (Anzidei et al., 2009; D'Agostino et al., 2012; Gualandi et al., 2014) outline a volume of activity ~ 40 km wide and ~ 9 km deep, as defined by the occurrence of repeaters at the seismicity cut-off

depth. At this depth a gently SW detachment was clearly identified as a major rheological discontinuity – probably a reactivated thrust or other inherited feature of the orogenic edifice (Di Luccio et al., 2010) – characterized by a dominantly creeping behaviour (Chiaraluce et al., 2011, 2012; Valoroso et al., 2013). A slow-slip event with a total moment release equivalent to a Mw ~ 5.9 earthquake and a duration of almost two weeks, interpreted to have originated along this detachment on 12 February 2009, would have eventually loaded the largest (magnitude 4.0) foreshock and the Mw 6.3 main shock (Borghi et al., 2016). Irrespective of the controversial occurrence of such a slow-slip event, it is worth noting that: (i) the occurrence of a sub-horizontal detachment at ~ 9 km depth is well constrained by seismological data (Chiaraluce et al., 2011, 2012; Valoroso et al., 2013), and (ii) the foreshocks extended far away from the main-shock fault rupture and over an area even larger in size than that of the aftershock sequence (Borghi et al., 2016). Furthermore, the temporal variations of seismic velocity and anisotropy revealed substantial changes in the elastic properties of the medium during the preparatory phase of the main shock (Lucente et al., 2010), for which a major role of overpressured fluids has been suggested (Di Luccio et al., 2010; Terakawa et al., 2010). Indeed, anomalously intense fluid circulation and strong gas emissions generally follow earthquakes in the Apennines (Italiano et al., 2004; Lombardi et al., 2010), showing a clear relationship with active fault segments (Ciotoli et al., 2014; Ascione et al., 2018). In the area of the 1980, M_S = 6.9 Irpinia earthquake in southern Italy, a high V_P/V_S ratio recorded by seismic tomography provides evidence for fluid reservoirs at hypocentral depths (Amoroso et al., 2014), where the occurrence of a fracture system saturated by brine-CO_2/CH_4 or CO_2-CH_4 mixtures has been inferred (Amoroso et al., 2017). The strongly anisotropic structure of fold and thrust belts like the Apennines, including late-orogenic low-angle normal faults and inherited Mesozoic extensional features besides gently dipping thrusts (e.g. Chiarabba et al., 2010), result in a layered architecture facilitating CO_2

accumulation in overpressurized reservoirs at depths ranging from few to c. 15 km (e.g. Chiodini et al., 2013). The actual occurrence of relatively shallow CO_2 reservoirs in the Apennines is shown by direct evidence, provided by deep boreholes, of fluids trapped at near-lithostatic pressures (Chiodini and Cioni, 1989). In particular, two deep wells, San Donato (Fig. 1) and Pieve Santo Stefano, encountered CO_2 pressures of about 98 and 67 MPa at depths of 4750 and 3700 m b.s.l., respectively (i.e., ~0.8 of the lithostatic pressure). Near-lithostatic pore pressure (CO_2) measured in the San Donato borehole was encountered in Triassic evaporites and just below the seal of a sub-horizontal thrust (Miller et al., 2004). A sudden upward migration of CO_2 followed the two mainshocks (of magnitude 5.7 and 6.0, nine hours apart; Miller et al., 2004) of the 1997 Colfiorito earthquake sequence, which occurred c. 80 km north of our study area (Fig. 1). Such mainshocks provided a transient connection with the uppermost crustal levels (at hydrostatic pore pressures) driving aftershock activity, with thousands of aftershocks that included four additional events with magnitudes between 5 and 6. Earthquake triggering by trapped, gas-rich (CO_2) fluids has been proposed based on various geophysical datasets also for the 2009 L'Aquila seismic sequence (Di Luccio et al., 2010). Here, strong evidences for the presence of overpressured fluids near the foreshocks and mainshock (Lucente et al., 2010; Savage et al., 2010; Terakawa et al., 2010) suggest that they contributed to the mainshock rupture (Picozzi et al, 2019). This also indicates the occurrence of a relatively shallow CO_2 reservoir, similar to that encountered in the San Donato borehole, besides the deep crustal one inferred by Chiodini et al. (2013) based on V_P anomaly and V_P/V_S ratio. The inferred role of CO_2 in earthquake nucleation is consistent with the fact that, at hypocentral depths, gases more than liquids may significantly increase the pore pressure, up to a level for which it equals the lithostatic pressure (Hantschel and Kauerauf, 2009). Transient pore pressure build up may also produce detectable ground deformation in the vicinity of earthquakes (Rossi et al., 2016).

In this study we show that preseismic ground deformation on a yearly time scale, revealed by multi-temporal Permanent Scatterers Synthetic Aperture Radar Interferometry (PS-InSAR), affected the region struck by the Mw 6.3, 2009 L'Aquila earthquake. In order to obtain a comprehensive picture of the pre-seismic deformation scenario, we have analysed PS data obtained from satellites ascending and descending tracks recorded in a more than 20 years long time period spanning over the 2009 L'Aquila earthquake. As GPS data highlighted transient, hydrologically-related horizontal deformations associated with recharge/discharge phases of aquifers in the Apennines (e.g., Devoti et al., 2018), a relevant rainfall dataset is also analysed in order to define to what extent the precipitation regime affected the observed preseismic ground motion.

Study area

The study area is located along the Apennine mountain chain, a Neogene fold and thrust belt forming the backbone of peninsular Italy (e.g. Butler et al., 2004) and presently undergoing post-orogenic extension (e.g. Cinque et al., 1993; Hippolyte et al., 1994; Cello et al., 1982, 1998; Ascione et al., 2013; Valente et al., 2019). Quaternary normal faults dissecting the axial zone of the mountain belt control active tectonics and seismicity of the study area (e.g., Di Luccio et al., 2010; Galli et al., 2010; 2011). At the surface, the Mw 6.3, 6th April 2009 L'Aquila main shock activated the Paganica Fault (hereinafter, PF), a ~20 km long structure composed of several *en-echelon*, SW-dipping segments, which bounds to the NE the Aterno valley Quaternary basin (Galli et al., 2010; 2011; Santo et al., 2014; Fig. 1). Besides surface faulting along the PF, the 2009 earthquake caused widespread ground ruptures in the L'Aquila region (Boncio et al., 2009; Falcucci et al., 2009; EMERGEO Working Group, 2010). Although coseismic deformation was imaged by geodetic and remote sensing methods (Anzidei et al., 2009; Cirella et al., 2009; Atzori et al., 2009; Walters et al., 2009;

Papanikolaou et al., 2010; Costantini et al., 2017), which contributed constraining the source characteristics of the 6th April 2009 main shock, only negligible pre-seismic ground displacement was detected to date over longer time windows by both GPS (Devoti et al., 2018) and InSAR data (Lanari et al., 2010; Atzori et al., 2013; Luo et al., 2013). It is worth noting that only two GPS stations (INGP and AQUI) provide a continuous record covering a multi-year preseismic period, while the SAR-based preseismic investigations were carried out using exclusively images recorded along satellite ascending orbits. Those investigations were based on images by the ALOS satellite in years 2005-2009 (Atzori et al., 2013) and by the Envisat satellite recorded in the 2003-2010 (Lanari et al., 2010) and October 2008 – September 2009 (Luo et al., 2013) time spans. By their analisys of PS time series, Luo et al. (2013) inferred a slow pre-seismic surface change (LoS-oriented negative followed by positive motions) in the area of the earthquake epicentre.

Methods and materials

SAR multi-temporal interferometric data analysis

Differential interferometry is based on the multi-temporal acquisition of interferometric Synthetic Aperture Radar (SAR) images, which allows measurement of ground deformations through the detection of phase variations of the electromagnetic signal along the radar spacecraft Line of Sight (LoS; Fig. S1). Numerous InSAR time series methods exist, including PS-InSAR (Permanent Scatterer technique; Ferretti et al., 2000; 2001) or PSP-DIFSAR (Persistent Scatterers Pairs – DIFSAR; Costantini et al., 2017). Permanent or Persistent Scatterers are man-made (structures on the roofs of buildings, utility poles, dams, etc.) or natural (rock outcrops), high radar reflecting objects for which spectral response does not change significantly during different acquisitions, as they are characterised by stable electromagnetic radar phase signal over long time series of InSAR images. Dispersion due to

temporal and geometrical decorrelation phenomena is thus minimized using PS as measurement points. When a significant number of independent radar phase stable points (PS) exists within a radar scene and enough radar acquisitions have been collected, displacement time series and displacement rates of each PS can be calculated along the SAR Line of Sight (LoS) with respect to a reference point, which is supposed to reflect an undeforming point (Hooper et al., 2004). The phase data from PSs are used to detect temporal changes of the ground surface.

This study is based on multi-temporal analysis of PS-datasets processed by images recorded along both the ascending and descending orbits by ERS and Envisat satellites, and along the descending orbit by COSMO-SkyMed satellite. PS-datasets analysed with this study were obtained from the Geoportale Nazionale of the Italian Ministry of Environment (MATTM) database (www.pcn.minambiente.it/mattm) and they were pre-processed with PSInSAR technique by the TRE® Company, and PSP-DIFSAR technique by the e-GEOS® Company. Details on the signal processing chain and related techniques are available in Costantini et al. (2015) and Costantini et al. (2017), and reference therein. The analysed datasets, which are listed in Table 1, are ERS (1991 - 2000), Envisat (2003 - 2010) and COSMO-SkyMed (2011 – 2014) PS data spanning over a 400 km^2 wide region centred on the L'Aquila 2009 earthquake epicentre. They consist of: (1) PS ERS data from the descending and ascending tracks, which are ~ 26000 and 14000 with average spatial distributions of 65 PS km^{-2} and 35 PS km^{-2}, respectively; (2) PS Envisat data from the descending and ascending tracks, which are ~ 44900 and 52700 with average spatial distributions of 100 PSkm^{-2} and 130 PS km^{-2}, respectively; (3) PS COSMO-SkyMed data from the descending track (PS data from the ascending orbit are not available to date), which are ~ 663×10^3 with an average spatial distribution of 1650 PS km^{-2}. The analysed ERS, Envisat and COSMO-SkyMed PS data have been processed and corrected for atmospheric and orbital artefacts. These are high quality

data (mean value of coherence index ~ 0.7), with standard deviations of PS mean velocity in the 0.4 - 0.5 mm yr^{-1} range, and of the deformation measurement error of ±3 mm, respectively (Costantini et al., 2015, 2017 and references therein).

Overall, the PS data analysis and processing consist of: (i) visual analysis of PS time series; (ii) statistical analysis of PS time series; (iii) evaluation of vertical and horizontal components of displacement summed up during different time spans; (iv) GIS geospatial data analysis by Arcgis®, used to construct a series of raster maps synthesising the spatial distribution of various parameters (e.g., LoS-oriented displacements/mean velocity, vertical/horizontal displacement components) at different time spans. For the geospatial analysis, the Inverse Distance Weighting interpolator (IDW) statistics with 50×50 m cell size is used.

There is only one COSMO-SkyMed descending orbit PS dataset available. This is used to obtain information on the postseismic behaviour of the study area in terms of spatial distribution of LoS-oriented mean velocities in the 2011 - 2014 time interval, which is assessed through geospatial analysis.

Indepth investigation of preseismic ground motions is performed by a thoroughly visual analysis of ERS and Envisat PS time series from both the ascending and descending orbit. For part of the analysed datasets – namely, part of the PS time series from the descending orbit – the careful inspection of Envisat PS time series allows the identification of up to four distinct stages, each one characterised by a rather uniform average velocity relative to the satellite. Based on such evidence, the Envisat time series from the entire investigated region are split at the dates separating the different stages, and the velocity/displacement PS data for each stage are analysed through geospatial analysis in order to identify areas featuring homogeneous motions.

As for the Envisat records both the ascending and descending datasets are available, data processing is performed in order to evaluate, for the identified four stages: (i) the vertical and

horizontal components of motion of single PS; (ii) the spatial distribution of vertical and horizontal ground motion components in the entire study region. Due to the near-polar orientation of satellite orbits, horizontal components of ground motion oriented N-S are poorly detected, and thus difficult to determine using SAR data, while determinations of the E-W oriented and vertical components are affected by a much smaller error, particularly when data from the ascending plus descending orbits are combined (e.g., Wright et al., 2014). Starting from PS motion recorded along SAR both ascending and descending orbits, we reconstruct 2D displacements/velocities in the vertical plane (z) oriented E-W (Fig. S1) through the evaluation of the vertical (*Dz* or *Vz*) and horizontal (E-oriented, *Deast* or *Veast*) components of PS displacement, or velocity, using equations [1] and [2], and [3] and [4] (Lündgren *et al.*, 2004; Manzo et al. 2006; Lanari et al., 2007; Tofani et al., 2013), respectively:

$$[1] \quad Dz = (DLoSd + DLoSa)/2\cos\phi$$

$$[2] \quad Deast = (DLoSd - DLoSa)/2\sin\phi$$

$$[3] \quad Vz = (VLoSd + VLoSa)/2\cos\phi$$

$$[4] \quad Veast = (VLoSd - VLoSa)/2\sin\phi$$

Where: $DLoSd$ and $DLoSa$ are PS displacement values oriented along the descending and ascending LoS, respectively; $VLoSd$ and $VLoSa$ are PS velocity values oriented along the descending and ascending LoS, respectively; ϕ is the LoS angle of incidence, which is approximately around 23° for ERS and Envisat satellites (Fig. S1; Table 1), and around 32° for the COSMO-SkyMed satellite. However, for Envisat and ERS satellites the incidence angle can vary across a radar scene by up to 8° around the middle value of 23°. We apply equations [1] and [2] to deconvolve the Envisat datasets and obtain values of Dz and $Deast$. The extent to which the variation of the incidence angle within a radar scene affects the derived displacement components, tested for a number of PS data, proves to be very limited

(the variations of the obtained Dz and $Deast$ are of the order of 10^{-1} mm). We consider negligible such a variation (which is one order of magnitude less than the obtained Dz and $Deast$ values) and use $\phi = 23°$ in equations [1] and [2].

The geometrical composition expressed in equations [1] and [2] rests on the availability of pairs of PS from images recorded by ascending and descending satellite tracks. However, (i) SAR images from the ascending and descending orbits are not temporally continuous, and (ii) in general, PS from ascending and descending images are not spatially coincident. As a consequence, in order to obtain couples of images useful to the deconvolution, we carefully analyse the available images and select ascending and descending orbit images characterised by both a good spatial matching of PS (tested through GIS-aided analysis) and limited time separation, which we set at one month. By such a strict selection process, we end with the composition of 24 ascending+descending radar image couples, which cover the 2005 – 2010 time span. The 24 selected image pairs are processed following equations [1] and [2] through geo-spatial analysis in order to construct a set of raster maps that show the spatial distribution of values of the vertical (z, up - down) and horizontal (east-west) components of the displacement vector summed up at each of the identified four stages. We use pre-processed products derived from an Advanced Differential SAR Interferometry approach (A-DInSAR) that significantly increases the potential of SAR remote sensing for ground deformation detection. The applied combination technique is conventional (Manzo et al., 2006), as other methods (e.g. Small BAselines Subset – SBAS, SqueeSAR; Berardino et al., 2002; Ferretti et al., 2011) exist to combine multi-satellite data for obtaining 2D displacement time-series (Samsonov and d'Oreye, 2012; Pepe et al., 2016). Within this context, the assumption that one-month separation datasets are sufficient to retrieve the 2D displacement time-series can be critical, especially in the case of an earthquake. However, as the main focus of this study is the long-time behaviour during the pre-seismic stage, the applied conventional approach is

fully adequate. In fact, using the PS method, it is possible to resolve surface motions of the order of ~ 0.5 mm yr^{-1}, a level of accuracy not reached by other techniques of SAR interferometry (Ferretti et al., 2007).

Maps showing the vertical component of displacement are used for the construction of profiles along traces oriented transverse to the main structures in the study area, which synthesise the vertical displacement summed up during each of the preseismic and coseismic time intervals set based on the results of the Envisat PS time series analysis. The uplifted/subsided rock volumes are evaluated using the 'Surface Volume' tool of the Arcgis® software, which calculates the volume of the region between a given surface and a reference plane (where each PS has an initial vertical deformation value equal to 0).

Statistical analysis of PS-InSAR data

Based on the results of the time series visual analysis, statistical analyses for trend detection based on both parametric and non-parametric approaches are carried out on the Envisat PS time series in order to evaluate the significance of the LoS-oriented preseismic displacements. The statistical analysis of the Envisat PS data from both ascending and descending tracks is focused on the area that – based on the results of the geospatial analysis – was affected by distinct preseismic deformation. For the parametric approach, the regression analysis is applied to the 2003 to March 2009 record of 52714 PS time series (40 data points) from the ascending orbit, and to the 2003 to September 2008 interval of 44950 PS time series (29 data points) from the descending orbit. For each point, the displacement is regressed against time. As routinely done in statistical analysis, the null hypothesis is tested. In our instance, the null hypothesis states that there is not significant linear displacement trend during the considered time span. The null-hypothesis stating that there is no difference between regression mean square and mean square error (i.e. there is not a significant linear

displacement trend during the considered time span) is tested by a F-test, with a significance level of 0.05 (Supplemental Table S1). The assumptions of normality and non-autocorrelation of residuals are checked using two-tailed Lilliefors test and Durbin-Watson test, respectively (Table S1).

The non-parametric trend analysis is based on Mann-Kendall test (two-tailed; Table S1) and Theil-Sen's slope estimation. Analysed PS datasets correspond to those investigated through the parametric trend analysis cover. The null hypothesis of trend absence is checked with a significance level of α=0.05.

Rainfall data analysis

Rainfall data used in this study were recorded at the 'L'Aquila S. Elia' meteorological station (Latitude: 42°20'03'', Longitude: 13°25'43''; elevation: 590 m a.s.l.), and cover the 2000-2018 time span. The rainfall time series consists of 666050 quarter-hour measurements, from which 228 monthly precipitation values are obtained. The monthly precipitation record is analysed through non-parametric trend analysis based on the Mann-Kendall test. The null-hypothesis of trend absence is checked at a α=0.05 level of significance. The cyclicity in the time series is analysed by means of a periodogram based on monthly precipitation. Cumulative rainfall data are detrended through a linear fit in order to examine long-term variations in the precipitation regime. Statistical analyses are performed by means of MATLAB® routines.

Topography analysis

A 10 m digital elevation model (Tarquini et al., 2012) is used for topography representation in the maps and construction of the profile of Fig. 10. The SRTM Nasa 90m DEM (Farr et al., 2000, 2007) is used for the construction of the swath profile by means of the

SwathProfiler Add-in of Arcgis® following the methodology by Pérez-Peña et al. (2017). Mean elevation values of the blocks in the NE and SW of the Paganica Fault are evaluated in 3D through a GIS-aided procedure over symmetrical, roughly square areas having one side corresponding to the Paganica Fault trace and lengths equivalent to about half (~ 20 km) of the swath profile length.

Results

PS multitemporal interferometry

An in depth inspection of all of the available time series of PS motion oriented along both the ascending and descending satellite Line of Sight (LoS; Fig. S1) was carried out. The analysed PS data are characterised by time-variable, small-amplitude motions. Such features may be related to the combination of apparent ground motion due to atmospheric artefacts (Hanseen, 2001), which are responsible for irregular – noisy – components (e.g., Vilardo et al., 2009; Atzori et al., 2013; Costantini et al., 2017), and short-period motions, which may include a hydrological component (Devoti et al., 2018).

Short-period and irregular ground motions in the range of ~ ±10 mm are the main feature of ERS PS time series from the entire study region. Such fluctuations are superposed on a sub-horizontal long-term trend (Figures S2 and S3), which indicates substantial absence of net ground displacements relative to satellite over the whole 2009 earthquake region in the 1992 – 2000 time span. Some fluctuations affect also the Envisat and COSMO-SkyMed PS time series, however they are subordinate in terms of magnitude and temporal persistence with respect to yearly-scale linear trends.

Envisat PS time series image a consistent temporal evolution, and spatial distribution, of ground motions on a yearly time scale. Different motion patterns are identified by the visual inspection of the ascending vs. descending orbit data, particularly for the region located to the

SW of the PF trace. The different motion patterns identified by the visual analysis of the PS time series are clearly imaged by the diagrams of Fig. 2, which show the spatial distribution of the ascending and descending LoS-oriented displacement vs. time for a high number of PS located along a transect (transect A, located in Fig. 1) oblique to the PF trace. The trace of transect A (300 m buffered) was selected based on the occurrence of a very dense spatial distribution of PS from both the ascending and descending tracks along its length. The ascending orbit PS time series show a sudden coseismic collapse of a wide area located SW of the PF, which is clearly imaged in the transect of Fig. 2a up to a distance of c. 15 km to the west of the fault. However, the PS time series from the ascending orbit do not show any net displacement trend relative to satellite throughout both the preseismic and post-seismic time spans in the entire region (e.g., Fig. 2a; Fig. S4).

Features of PS time series from the Envisat descending tracks are more spatially and temporally variable. In particular, the visual inspection of the huge amount of PS time series distributed over a wide region located to the SW of the PF allowed us to distinguish, in the time span predating the coseismic collapse, an upward, LoS oriented motion trend (2002 to September/October 2008, hereinafter Preseismic Stage 1), followed by a comparable downward ground motion lasting until February 2009 (Preseismic Stage 2; Fig. 2b). This behaviour is clearly synthesised by the time series of PS located along transect A (Fig. 2b), which crosses the region to the SW of the PF from an essentially stable area, to the west, to the fault trace, to the east. In fact, as shown by the diagram of Fig. 2b, throughout the Preseismic Stage 1, the PS located along transect A up to a distance of c. 15 km from the PF are characterised by a motion towards the satellite with a rather constant average velocity in the range of few millimetres per year (Fig. S5). The segment of transect A affected by slow LoS-oriented positive motion is subsequently (i.e. during Preseismic Stage 2) subject to a faster motion away from the satellite, recorded during the October 2008 – February 2009

time span (Fig. 2b). Following coseismic collapse, a subdued postseismic negative motion is observed until the end of the Envisat record (June 2010) in the region to the SW of the PF, which includes transect A (Fig. 2b).

The subdued LoS-oriented motion patterns observed during the preseismic period by inspection of the PS time series from the Envisat descending orbit dataset were investigated in detail, and tested through statistical (parametric and non-parametric) trend analyses of both the ascending and descending PS time series from the area to the SW and NE of the PF. Such a testing was performed in order to verify that the magnitude of the observed deformation is not compatible with 'random' effects. The statistically analysed PS data are those located in the region in which, through the visual analysis of time series of PS from the descending orbit dataset, distinct preseismic displacement patterns were identified. The trend analysis was applied to the entire preseismic interval of the ascending orbit PS time series. For the descending orbit PS time series, only the time interval of Presesmic Stage 1, during which the average velocity is subdued, was investigated in detail. The results of the parametric trend analysis are shown in Fig. 2 and in Fig. 3. For most of the time series, both the assumption of normality of the residues and absence of auto-correlation are verified (Fig. 4). Comparison of Figures 3 and 5 shows that results of the parametric and non-parametric trend analyses are almost matching. The analyses of PS data obtained by the Envisat ascending orbit indicate non-significant preseismic deformation trends (Fig. 2a; Figures 3 and 5), thus confirming the outcomes of the visual inspection of the time series. By converse, analyses of the descending orbit dataset shows clear evidence of significant deformation in the 2002 to September 2008 time span and, also in this case, confirm the existence of positive LoS-oriented displacement in the region to the SW of the PF during the Preseismic Stage 1 (Figures 3 and 5; Fig. 2b). Eastwards of the PF, the results of both the parametric and non-parametric trend analyses are

less straightforward. However, preseismic negative deformation trends tend to be prevailing (Fig. 3).

Statistical analysis of rainfall data

In order to test to what extent the PS time series are related to the rainfall regime, a statistical analysis of rainfall data was carried out on the precipitation time series, which cover a time interval spanning from 2000 to 2018. In the rainfall data, no significant trend was identified for both the entire time series and for the narrower time interval (2002-2009) corresponding with that covered by the analysed PS record. A comparison between the rainfall record and the PS-InSAR time series computed from 200 data points located in the area around the 'L'Aquila S. Elia' meteorological station, clearly highlights a lack of correspondence between the rainfall and both the ascending and descending time series (Fig. 6). In the entire 2000-2018 time interval, cycles of about 6, 12, and 57 months were identified (Fig. 7). The identified cyclicity clearly produces autocorrelation in the monthly precipitation anomalies (Fig. 6). In contrast, the regression residuals of PS-InSAR data do not show any significant autocorrelation (Fig. 4). This indicates that a linear model adequately fits the PS-InSAR time series, further supporting the absence of any significant systematic effect of the cyclically varying precipitations on the ground deformation trends in our case study. When the long-term variations in the precipitation regime are considered, it may be noted that the detrended cumulative rainfall data curve shows a decrease starting from the spring of year 2006 (diagram d of Fig. 6). Such a decrease does not correlate with both the descending PS time series, which show a steady average velocity throughout the 2002-October 2008 time span (diagram a in Fig. 6), and the ascending PS time series, which show a substantially null velocity until the 6th April 2009 earthquake occurrence (diagram b of Fig. 6).

Time-space distribution of ground motions

Displacement components oriented along both the ascending and descending satellite LoS were combined following equations [1] and [2] in order to estimate spatially distributed vertical and horizontal (E-W oriented) components of ground displacements at distinct time spans. The spatial distribution of pre- to post-seismic ground deformation (in terms of vertical and horizontal components) in the entire study region is synthesised in the maps of Fig. 8. Based on the outcomes of time series inspection, the pre-seismic time span has been split into Preseismic Stage 1 and Preseismic Stage 2. For both the preseismic and postseismic time spans, the ground motion patterns recorded by Envisat along the ascending and descending orbits are different. Such differences appear as the response to the SAR acquisition geometry (e.g., insets in Fig. 3; Fig. S1). In fact, while purely vertical PS motion is expressed more or less equally in both the ascending and descending LoS (Fig. S1), east or west oriented ground motions occurring along a plane dipping at a high angle (~ 90°) with respect to that of the LoS are not sensed along that LoS (Fig. S1).

The maps of Fig. 8 show that, during Preseismic Stage 1, a large area to the SW of the PF experienced uplift and eastward oriented displacement (Fig. 8a), with mean and maximum uplift values of ~10 mm and 25 mm, respectively, and mean displacement towards the descending orbit in the +18±6 mm range. The uplifted area is much wider than the Aterno valley basin (Fig. 1), and encompasses both topographic highs and lows, although its mean elevation value of 983 m is lower than the 1319 m mean elevation value of the block to the NE of the PF. During Preseismic Stage 2 (Fig. 8b), the same area that in the former time span had been uplifted underwent negative vertical displacement with a mean value of ~10 mm (and corresponding mean displacement towards satellite in the -14±6 mm range) with horizontal component oriented towards the west. In the coseismic time span, sudden collapse with maximum values in the 180 – 200 mm range (and mean value ~ 80 mm) focused to the

SW of the PF, but involving also part of the area to the NE of the PF, is imaged in the map of Fig. 8c, along with slight uplift of the surrounding region. The early postseismic displacement field is characterised by subdued subsidence focused to the SW of the PF (Fig. 8d). Overall, the hanging-wall volume subsided in the coseismic to early post-seismic stages (i.e. subsidence recorded between April and May 2009) is of ~ 24.5×10^6 m^3, while the volume uplifted during the same time span is of ~ 55×10^3 m^3 (Fig. 9). The map of Fig. 8e shows negative velocity values relative to the COSMO-SkyMed descending orbit in the region to the SW of the PF continuing until 2014.

The profiles of Fig. 10 synthesise the time-space evolution of vertical displacements along a transect crossing the PF. The profiles show that the trace of the PF falls in the highest gradient segment between the block to the southwest, which experienced E-oriented uplift during Preseismic Stage 1 and W-oriented subsidence during Preseismic Stage 2, and the initially lowered and then uplifted block to the northeast. A complex deformation pattern is highlighted by the lowest profile of Fig. 10, which shows that the area affected by coseismic collapse includes part of the elevations to the SW and NE of the Aterno river valley.

Discussion

The results of this study unravel a peculiar pattern of ground motion in the epicentral area of the 2009 L'Aquila earthquake, starting several years before the onset of the seismic sequence. Our findings on the co- to early post-seismic vertical ground displacements are consistent with those provided by former studies based on geodetic and SAR data (Atzori et al., 2009; Cirella et al., 2009; Walters et al., 2009; Cheloni et al., 2010), and with the GPS record (e.g., Blewitt et al., 2018) provided by the stations INGP and AQUI (Fig. 8). Our results also show that the collapsed area extends towards the NE beyond the PF trace, and allow the detection of several steps in the displacement profile (Fig. 10). These might indicate subdued ruptures

along two belts, also hosting active fault strands (Pierantoni et al., 2017), located to the SW and NE of the area affected by maximum subsidence. Consistent with evidence from GPS data (D'Agostino et al., 2012), postseismic subsidence in the hanging wall of the PF is recognised by combined ascending/descending orbits Envisat data. In addition, based on COSMO-SkyMed data we analysed, a persistence of hanging-wall negative ground displacements at least through year 2014 may be inferred. This is consistent with previous studies on postseismic deformation, which point out that surface deformation may continue for years or even decades as a result of postseismic afterslip (e.g. Copley, 2012; Ascione et al., 2020).

Regarding the preseismic period, no significant displacement was detected in the 1992 - 2000 time interval by PS time series obtained from the ERS satellite records. Similarly, no significant pre-sesimic LoS-oriented displacement was highlighted by inspection and statistical analysis of the Envisat ascending data set spanning on years 2003-2010, consistent with the results of the analysis by Lanari et al. (2010) of that same data set we analysed. In addition, the surface change reported by Luo et al. (2013) is not highlighted by our analysis. In particular, our inspection of the Envisat PS time series from the area affected by coseismic collapse (where ~43000 ascending orbit PS are located) indicates that LoS-oriented fluctuations in the range of those reported by Luo et al. (2013), i.e. negative displacements with maximum values in the range of -15 to -28 mm and maximum positive displacements in the ~10 – 25 mm range from October to November 2008, affected only limited amounts of PS (91 and about 200, respectively). Spotty and temporally-limited positive/negative displacements comparable to those described so far are recorded both before and after year 2008 (e.g., Fig. S4), therefore resulting as non-significant based on our long-term analysis.

Our analysis of the PS time series from the descending orbit highlighted changes in the average LoS-oriented velocity in a large region to the SW of the Paganica Fault. We interpret

the apparent inconsistency represented by the different patterns of ground motion recorded by coeval ascending and descending tracks as an effect of the geometry of the satellite orbits relative to the displacement of the ground surface, as it is commonly observed where a horizontal (E–W oriented) component of motion contributes to ground deformation (e.g., Manzo et al., 2006; Jolivet et al., 2012; Jin et al., 2017). Ground motion may be even undetectable along one of the orbits if it occurs within a plane roughly orthogonal to the satellite LoS (Fig. S1). Therefore, the combination of the ascending and descending datasets allowed us constraining the 2D orientations of the pre- and post-seismic displacement vectors. In this regard, we note that images by Atzori et al. (2013; their Figure 5) reveal a pre-seismic positive displacement (motion towards the satellite) from September 2007 to July 2008 recorded by the ascending track of the ALOS satellite. The different motion patterns imaged by the Envisat and ALOS ascending orbits during the same time span appears as the response of their different viewing geometries, and supports our interpretation on the control exerted by the orientation of the viewing geometry relative to ground motion vectors. In fact, the LoS of ALOS is less inclined (~11° relative to the vertical axis) with respect to the Envisat LoS (~23°).

Interpretation of ground motion

The multi-temporal, spatial analysis of ground deformation performed by the analysis of PS interferometric datasets unravelled a peculiar pattern of ground deformation predating the 2009 L'Aquila earthquake. In particular, temporally and spatially distributed preseismic motions since the end part of year 2002 have been detected. During these preseismic ground deformation stages, the PF marks the boundary between two blocks that experienced motions with opposite orientations of the vertical and horizontal components. The sector corresponding to the PF hanging-wall block experienced uplift with east-directed motion,

followed by subsidence with west-directed movement. Values of cumulative vertical ground displacements (averaged over the entire uplifted/subsided area) during Preseismic Stages 1 and 2 are comparable, both being of ~10 mm, thus suggesting a common source for the observed preseismic deformation. The combined vertical and horizontal components point to slow reverse-fault motion along the PF during Preseismic Stage 1, followed by normal-fault motion along the PF during Preseismic Stage 2. Reverse-fault motion during Preseismic Stage 1 started about 6 years before the April 2009 main shock and was coeval with subdued subsidence of the PF footwall block (Fig. 8; Fig. 10). Up/down and E/W reversals of displacements affecting the blocks separated by the PF occurred 6-8 months prior to the April 2009 main shock (Preseismic Stage 2; Fig. 8; Fig. 10). The multi-year nature of the deformation cycles outlined in this study clearly rules out a significant impact of hydrologically-related seasonal deformations. It is worth noting that climatically-controlled recharge of the aquifers has been related to multi-year, widespread transient deformation observed at all the GPS stations along the Apennines close to carbonate rock (Devoti et al., 2018; Silverii et al., 2019). However, the pattern pointed out by these latter studies is homogeneous over a very large area, whereas the pattern outlined in this study is characterized by opposite uplift/subsidence motions of much larger magnitude affecting two well defined blocks (i.e. hanging wall and footwall) bounded by the PF. This composite, articulated deformation pattern is independent from that associated with hydrological processes (Devoti et al., 2018) and, due to its clear relationship with structural features and architecture, is best related with tectonic processes. Available GPS data from the study area come from the INGP and AQUI stations (Fig. 8). These stations are located in the western portion of the PF termination zone, therefore outside the area characterised by strong preseismic deformation outlined by the InSAR data in this study (Fig. 8). As a consequence, the lack of any significant preseismic trend in the GPS-detected vertical motion (Blewitt et

al., 2018) is consistent with InSAR-derived information from the same two sites. Furthermore, the northward velocity vectors provided by GPS measurements for our study area (Devoti et al., 2017) are hardly detectable by InSAR data due to the near-polar orientation of SAR orbits (e.g., Lündgren et al., 2004; Wright et al., 2014). On the other hand, the correlation between GPS-detected horizontal motion anomalies from these two sites and rainfall cyclicity outlined by Devoti et al. (2018) involves movements that are one order of magnitude smaller (i.e., 10^0 vs. 10^1 mm) than those detected by the InSAR in the area characterised by strong preseismic deformation (Fig. 8). This confirms the dominant role played by tectonic deformation in the detected InSAR preseismic ground motion, while hydrologically related deformation is likely to represent a regional background signal that is clearly subordinate within the earthquake epicentral area and does not significantly affect the trend outlined in this work. Indeed, the statistical comparison of the rainfall regime with the PS-InSAR data carried out in this study highlights that the two signals are unrelated (Fig. 6). As the two GPS stations are located in a marginal portion of the PF hanging wall, InSAR results are fundamental for unravelling surface deformation surrounding the fault. The PF exerts a clear control on the pattern of recorded ground motions in the study area, as its surface trace bounds sectors characterized by contrasting behaviours during the investigated pre- to post-seismic stages.

The preseismic motions of the PF hanging wall identified in this study suggest a relationship of the surface deformation field with seismic phenomena. Such a relationship is inferred from the spatial correlation of the region affected by ground motion reversal with that containing the mainshock and most of epicentres of the seismic sequence (Valoroso et al., 2013), and from the chronological correlation of the preseismic inversion of ground displacements with the beginning of the foreshocks (October 2008; Di Luccio et al., 2010). As the spatial scale of this region is independent from surface geology features other than the PF, deep-seated

causative mechanisms for the preseismic motions such as volume changes related to lateral/vertical fluid migration and fracturing processes at depth may be inferred. Such processes have been suggested in association with the occurrence of the 2009 L'Aquila earthquake (Lucente et al., 2010; Chiaraluce et al., 2011; Moro et al., 2017).

Implications for the seismic cycle

The inferred seismic cycle explaining the observed ground motions is shown in Fig. 11. The proposed interpretation is independent of the actual occurrence of the sub-horizontal detachment portrayed in Fig. 11, as our model is based on the widely accepted concept of stick-slip fault behaviour in the upper crust and on the presence of a stable sliding fault in the middle-lower crust (Doglioni et al., 2011, 2015; Petricca et al., 2015), irrespective of its actual geometry. During the inter-seismic stage, aseismic creep occurs along the basal gently dipping detachment or stable sliding fault at depth, while the overlying shallow fault segment is locked. This leads to the development of a fractured volume located in the hanging wall of the fault. Fault zone fracturing, substantially lowering its sealing potential, together with hanging wall dilation, allow high-pressure CO_2 to flow from the footwall to the hanging wall (Fig. 11a). This process is attributed to the difference in lithostatic pressure on the top seal of the high-pressure CO_2 trap produced by the different mean topographic elevation of footwall and hanging-wall blocks. The measured mean elevation difference of 336 m results in a lithostatic pressure difference of c. 10 MPa on the top seal of the high-pressure CO_2 zone. Furthermore, numerical modelling of interseismic deformation indicates that the strain above the transition between the unlocked creeping detachment and the locked upper fault segment creates a dilated volume in the hanging wall and a contracted volume in the footwall (Albano et al., 2021). This produces pore pressure gradients triggering fluid flux from surrounding overpressurized CO_2 reservoirs. It is worth noting that this process may account for CO_2

flowing toward the dilated volume in the hanging wall even in case the fault retained a sealing potential and acted as a barrier for across-fault fluid flow, as in this instance the fluid input could also come along strike and/or from deeper reservoirs. Likewise, along-strike pathways may allow in this case drainage of the contracting footwall block.

As the CO_2 pressure in the hanging-wall block reaches a value able to counteract the lithostatic pressure, hanging-wall uplift occurs, with incipient unlocking of the fault. A porosity wave (i.e. a packet of fluid-filled interconnected cracks that self-propagates following the pressure gradient; Wiggins et al., 1995; Connolly and Podladchikov, 1998, 2013; Revil and Cathles, 2002) accommodates CO_2 migration from the footwall to the hanging wall of the locked non-sealing fault, or alternatively fluid arrival along strike and/or from depth below in case of a sealing fault. The porosity wave moves in the direction of minimum horizontal stress (NE-SW in the study area; D'Agostino et al., 2011) and upward, producing a transient displacement propagating through the region with an approximately elliptical pattern at the surface. The hanging-wall volume uplifted during the January 2003 - October 2008 time span (Preseismic Stage 1) amounts to ~ 2.24×10^6 m^3. Although higher amplitudes are observed in the vertical signal, the horizontal component of motion unravelled in this study indicates that upward hanging wall motion is accompanied by eastward displacement along the fault dip direction, implying the reactivation of the PF as a reverse fault (Fig. 11b).

Continuous slip along the basal detachment/creeping fault produces further cracks and dilation in the PF hanging wall, decreasing the pore fluid pressure that can no longer be counterbalanced by CO_2 flow from surrounding overpressured reservoirs. As the lithostatic pressure can no longer be sustained by the high-pressure CO_2, a reversal of motion occurs. This leads to normal fault-related hanging-wall subsidence (Fig. 11c), a process accompanied by extensional foreshocks during the L'Aquila sequence. The hanging-wall volume that

subsided during the October 2008 - March 2009 time span (Preseismic Stage 2) amounts to ~ 2.20 $\times 10^6$ m^3, therefore substantially balancing the uplift achieved during Preseismic Stage 1. Further hanging-wall dilation, produced by continued motion of the deep detachment/creeping fault, eventually leads to the catastrophic collapse of the hanging-wall block, generating the main shock (Doglioni et al., 2011, 2015; Petricca et al., 2015; Fig. 11d). This process is facilitated by the decreased fault strength as a result of its previous unlocking during both upward and downward hanging-wall motion in the pre-seismic stages. The coseismic to early post-seismic subsided hanging-wall volume is of ~ 24.5$\times 10^6$ m^3, while the coevally uplifted volume is of ~ 55$\times 10^3$ m^3 only (Fig. 9). A very large discrepancy between subsided and uplifted volumes is commonly observed in normal fault-related earthquakes, a feature that was recently attributed to the accommodation of coseismic strain by a stress-drop driven collapse of precursory dilatancy (Bignami et al., 2019). For the L'Aquila earthquake, the subsided area includes part of the footwall of the PF, while the uplifted area is located about 15 km SW of the PF, suggesting the possible occurrence of an antithetic normal fault at this location (Di Luccio et al., 2010; EMERGEO Working Group, 2010). Breaching the seal of the deep CO_2 trap provides a transient connection with the overlying shallow crustal levels, possibly driving aftershock activity (as in the case of the 1997 Colfiorito earthquake; Miller et al., 2004) and CO_2 flow toward the surface. This CO_2, feeding shallow aquifers (Chiodini et al., 2020), locally also gives rise to soil gas emissions (Lombardi et al., 2010; Quattrocchi et al., 2011; Ciotoli et al., 2014). The closure of residual fracture porosity produces further hanging-wall subsidence in the post-seismic stage (Fig. 11e). During this stage, minor downward motion affects also part of the footwall block, resulting in a larger subsiding area (Fig. 10). This process could be related with the upward escape of CO_2 from the breached deep trap, producing a decrease of pore fluid pressure and minor collapse of the footwall rock volume (Fig. 11e).

Conclusions

This study provides new, relevant insights into the use of long-term (yearly scale) multitemporal InSAR data analysis in the monitoring of active structures. Our results emphasize the pivotal importance of a correct choice of the time frame for a meaningful analysis of ground motions. In our instance, a significant tectonic signal is evident on the tens of year time scale. Observations on a short time window (e.g. Luo et al., 2013) may be inadequate to identify a significant trend, as clearly pointed out by the statistical analysis carried out in this study.

The detailed reconstruction of the seismic cycle of the 2009 L'Aquila earthquake is based on a comprehensive picture of ground deformation obtained by the analysis of PS data using image pairs from both ascending and descending orbits over a several-year time-frame. Preseismic ground displacements, pointing out a motion reversal of the PF hanging-wall block, provide a precursor signal of the 2009 Mw 6.3 earthquake. Given that the L'Aquila earthquake was driven by tectonic extension, the inferred transient volume changes at the base of the seismogenic fault may have modified the existing stress state enough to adjust the timing of the L'Aquila event, therefore acting as a trigger.

Acknowledgements

We are grateful to Ekbal Hussain, an Anonymous Reviewer and the Subject Editor Amy Gilligan for their thoughtful comments and suggestions. Fruitful discussions with Aldo Zollo, Gaetano Festa, Matteo Picozzi and Antonio Emolo are gratefully acknowledged. We kindly acknowledge Giancarlo Boscaino, Responsible of the Centro Funzionale e Ufficio Idrografico Regione Abruzzo - Dipartimento delle Opere Pubbliche, Governo del Territorio e Politiche Ambientali, for making the rainfall data available to us.

Conflict of interest: The authors declare no known conflicts of interest associated with this publication.

References

Albano M., Barba S., Bignami C., Carminati E., Doglioni C., Moro M., Stramondo S. & Saroli M. 2021. Three-dimensional numerical simulation of the interseismic and coseismic phases associated with the 6 April 2009, Mw 6.3 L'Aquila earthquake (Central Italy). *Tectonophysics*, **798**, 228685, doi: 10.1016/j.tecto.2020.228685

Amoroso, A., Russo, G., De Landro, G., Zollo, A., Garambois, S., Mazzoli, S., Parente, M. & Virieux, J. 2017. From Velocity and Attenuation Tomographies to Rock Physical Modeling: Inferences on fluid- driven earthquake processes at the Irpinia fault system in Southern Italy. *Geophysical Research Letters*, **44**, 6752–6760, doi: 10.1002/2016GL072346

Amoroso, O., Ascione, A., Mazzoli, S., Virieux, J. & Zollo, A. 2014. Seismic imaging of a fluid storage in the actively extending Apennine mountain belt, southern Italy. *Geophysical Research Letters*, **41**, 3802-3809, doi: 10.1002/2014GL060070

Anzidei, M., Boschi, E., Cannelli, V., Devoti, R., Esposito, A., Galvani, A., Melini, D., Pietrantonio, G., Riguzzi, F., Sepe, V. & Serpelloni, E. 2009. Coseismic deformation of the destructive April 6, 2009 L'Aquila earthquake (central Italy) from GPS data. *Geophysical Research Letters*, **36**, L17307, doi:10.1029/2009GL039145

Ascione, A., Ciotoli, G., Bigi, S., Buscher, J., Mazzoli, S., Ruggiero, L., Sciarra, A., Tartarello, M.C. & Valente, E. 2018. Assessing mantle vs. crustal sources for non-volcanic degassing along fault zones in the actively extending southern Apennines

mountain belt (Italy). *Geological Society of America Bulletin*, **130**, 1697-1722, https://doi.org/10.1130/B31869

Ascione, A., Mazzoli, S., Petrosino, P. & Valente, E. 2013. A decoupled kinematic model for active normal faults: Insights from the 1980, M_S = 6.9 Irpinia earthquake, southern Italy. *Geological Society of America Bulletin*, **125** (7-8), 1239-1259, doi: 10.1130/B30814.1

Ascione, A., Nardò, S. & Mazzoli, S. 2020. The MS 6.9, 1980 Irpinia Earthquake from the basement to the surface: a review of tectonic geomorphology and geophysical constraints, and new data on postseismic deformation. *Geosciences*, **10**, 493, doi:10.3390/geosciences10120493

Atzori, S., Hunstad, I., Chini, M., Salvi, S., Tolomei, C., Bignami, C., Stramondo, S., Trasatti, E., Antonioli, A. & Boschi, E. 2009. Finite fault inversion of DInSAR coseismic displacement of the 2009 L'Aquila earthquake (central Italy). *Geophysical Research Letters*, **36**, L15305, doi: 10.1029/2009GL039293

Atzori, S., Chiarabba, C., Devoti, R., Bonano, M. & Lanari, R. 2013. Anomalous far-field geodetic signature related to the 2009 L'Aquila (central Italy) earthquake. *Terra Nova*, **25**, 343–351, doi: 10.1111/ter.12040.

Berardino, P., Fornaro, G., Lanari, R. & Sansosti, E. 2002. A new Algorithm for Surface Deformation Monitoring based on Small Baseline Differential SAR Interferograms. *IEEE Transactions on Geoscience and Remote Sensing*, **40**, 2375-2383.

Bignami, C. Valerio, E., Carminati, E., Doglioni, C., Tizzani, P. & Lanari, R. 2019. Volume unbalance on the 2016 Amatrice-Norcia (Central Italy) seismic sequence and insights on normal fault earthquake mechanism. *Scientific Reports*, **9** (1), 4250.

Blewitt, G., Hammond, W.C. & Kreemer, C. 2018. Harnessing the GPS Data Explosion for Interdisciplinary Science. *Eos*, **99**, https://doi.org/10.1029/2018EO104623

Boncio, P., Pizzi, A., Brozzetti, F., Pomposo, G., Lavecchia, G., Di Naccio, D. & Ferrarini, F. 2010. Coseismic ground deformation of the 6 April 2009 L'Aquila earthquake (central Italy, Mw 6. 3). *Geophysical Research Letters*, **37**, L06308.

Borghi, A., Aoudia, A., Javed, F. & Barzaghi, R. 2016. Precursory slow-slip loaded the 2009 L'Aquila earthquake sequence. *Geophysical Journal International*, **205**, 776-784.

Butler, R.W.H., Mazzoli, S., Corrado, S., Donatis, M.D., Di Bucci, D. Gambini, R., Naso, G., Nicolai, C., Scrocca, D., Shiner, P. & Zucconi, V. 2004. Applying Thick-skinned Tectonic Models to the Apennine Thrust Belt of Italy—Limitations and Implications: in McClay, K.R., ed., Thrust tectonics and hydrocarbon system. *American Association of Petroleum Geologist Memoir*, **82**, 647–667.

Cello, G., Guerra, I., Tortorici, L., Turco, E. & Scarpa, R. 1982. Geometry of the neotectonic stress field in southern Italy: geological and seismological evidence. *Journal Structural Geology*, **4**, 385–393.

Cello, G., Mazzoli, S. & Tondi, E. 1998. The crustal fault structure responsible for the 1703 earthquake sequence of central Italy. *Journal of Geodynamics*, **26** (2-4), 443-460.

Cheloni, D., D'Agostino, N., D'Anastasio, E., Avallone, A., Mantenuto, S., Giuliani, R., Mattone, M., Calcaterra, S., Gambino, P., Dominici, D., Radicioni, F. & Fastellini, G. 2010. Coseismic and initial post-seismic slip of the 2009 Mw 6.3 L'Aquila earthquake, Italy, from GPS measurements. *Geophysical Journal International*, **181**, 1539–1546.

Chiarabba, C., Amato, A., Anselmi, M., Baccheschi, P., Bianchi, I., Cattaneo, M., Cecere, G., Chiaraluce, L., Ciaccio, M. G., De Gori, P., De Luca, G., Di Bona, M., Di Stefano, R., Faenza, L., Govoni, A., Improta, L., Lucente, F. P., Marchetti, A., Margheriti, L., Mele, F., Michelini, A., Monachesi, G., Moretti, M., Pastori, M., Piana Agostinetti, N., Piccinini, D., Roselli, P., Seccia, D. & Valoroso, L. 2009. The 2009 L'Aquila (central Italy) M_w 6.3

earthquake: Main shock and aftershocks. *Geophysical Research Letters*, **36**, L18308, doi: 10.1029/2009GL039627.

Chiarabba, C., Bagh, S., Bianchi, I., De Gori, P., & Barchi, M.R. 2010. Deep structural heterogeneities and the tectonic evolution of the Abruzzi region (Central Apennines, Italy) revealed by microseismicity, seismic tomography, and teleseismic receiver functions. *Earth and Planetary Science Letters*, **295**, 462–476.

Chiaraluce, L. 2012. Unravelling the complexity of Apenninic extensional fault systems: A review of the 2009 L'Aquila earthquake (Central Apennines, Italy). *Journal Structural Geology*, **42**, 2-18.

Chiaraluce, L., Valoroso, L., Piccinini, D., Di Stefano, R. & De Gori, P. 2011. The anatomy of the 2009 L'Aquila normal fault system (central Italy) imaged by high resolution foreshock and aftershock locations. *Journal of Geophysical Research: Solid Earth*, **116**, B12311, doi: 10.1029/2011JB008352

Chiodini, G. & Cioni, R. 1989. Gas geobarometry for hydrothermal systems and its application to some Italian geothermal areas. *Applied Geochemistry*, **4**, 465–472, doi: 10.1016/0883-2927(89)90004-8.

Chiodini, G., Cardellini, C., Caliro, S., Chiarabba, C. & Frondini, F. 2013. Advective heat transport associated with regional Earth degassing in central Apennine (Italy). *Earth and Planetary Science Letters*, **373**, 65–74.

Chiodini, G., Cardellini, C., Di Luccio, F., Selva, J., Frondini, F., Caliro, S., Rosiello, A., Beddini, G. & Ventura, G. (2020). Correlation between tectonic CO_2 Earth degassing and seismicity is revealed by a 10-year record in the Apennines, Italy. *Science advances*, **6** (35), eabc2938.

Cinque, A., Patacca, E., Scandone, P. & Tozzi, M. 1993. Quaternary kinematic evolution of the Southern Appennines. Relationships between surface geological features and deep lithospheric structures. *Annals of Geophysics,* **36** (2), 249-260.

Cinti, F.R., Cucci, L., Marra, F. & Montone, P. 2000. The 1997 Umbria-Marche earthquakes (Italy): relation between the surface tectonic breaks and the area of deformation. *Journal of Seismology,* **4**, 333-343.

Ciotoli, G., Bigi, S., Tartarello, C., Sacco, P., Lombardi, S., Ascione, A. & Mazzoli, S. 2014. Soil gas distribution in the main coseismic surface rupture zone of the 1980, Ms=6.9, Irpinia Earthquake (southern Italy). *Journal of Geophysical Research: Solid Earth,* **119**, 2440-2461, doi: 10.1002/2013JB010508

Cirella, A., Piatanesi, A., Cocco, M., Tinti, E., Scognamiglio, L., Michelini, A., Lomax, A. & Boschi, E. 2009. Rupture history of the 2009 L'Aquila (Italy) earthquake from non- linear joint inversion of strong motion and GPS data. *Geophysical Research Letters,* **36**, L19304, doi: 10.1029/2009GL039795

Connolly, J.A.D. & Podladchikov, Y.Y. 1998. Compaction-driven fluid flow in viscoelastic rock. *Geodinamica Acta*, **11**, 55-84.

Connolly, J.A.D. & Podladchikov, Y.Y. 2013. A hydromechanical model for lower crustal fluid flow. In Metasomatism and the chemical transformation of rock, 599-658 (Springer, Berlin, Heidelberg).

Copley, A., Hollingsworth, J. & Bergman, E. 2012. Constraints on fault and lithosphere rheology from the coseismic slip and postseismic afterslip of the 2006 Mw 7.0 Mozambique earthquake, *Journal of Geophysical* Research, **117**, B03404, doi:10.1029/2011JB008580.

Costantini, M., Minati, F., Ciminelli, M.G., Ferretti, A. & Costabile, S. 2015. Nationwide ground deformation monitoring by Persistent Scatterer Interferometry. In 2015 IEEE

International Geoscience and Remote Sensing Symposium (IGARSS) (pp. 1472-1475). IEEE.

Costantini, M., Ferretti, A., Minati, F., Falco, S., Trillo, F., Colombo, D., Novali, F., Malvarosa, F., Mammone, F., Vecchioli, F., Rucci, A., Fumagalli, A., Allievi, J., Ciminelli, M.G. & Costabile, S. 2017. Analysis of surface deformations over the whole Italian territory by interferometric processing of ERS, Envisat and COSMO-SkyMed radar data. *Remote Sensing of Environment*, **202**, 250-275.

D'Agostino, N., Cheloni, D., Fornaro, G., Giuliani, R. & Reale, D. 2012. Space-time distribution of afterslip following the 2009 L'Aquila earthquake. *Journal of Geophysical* Research, **117**, B02402.

D'Agostino, N., Mantenuto, S., D'Anastasio, E., Giuliani, R., Mattone, M., Calcaterra, S., Gambino, P. & Bonci, L. 2011. Evidence for localized active extension in the central Apennines (Italy) from global positioning system observations. *Geology*, **39**, 291-294.

Devoti, R., D'Agostino, N., Serpelloni, E., Pietrantonio, G., Riguzzi, F., Avallone, A., Cavaliere, A., Cheloni, D., Cecere, G., D.Ambrosio, C., Falco, L., Selvaggi, G., Métois, M., Esposito, A., Sepe, V., Galvani, A. & Anzidei, M. 2017. A combined velocity field of the Mediterranean region. *Annals of Geophysics*, **60** (2), 0215, doi:10.4401/ag-7059.

Devoti, R., Riguzzi, F., Cinti, F. R. & Ventura, G. 2018. Long-term strain oscillations related to the hydrological interaction between aquifers in intra-mountain basins: A case study from Apennines chain (Italy). *Earth and Planetary Science Letters*, **501**, 1-12.

Di Luccio, F., Ventura, G., Di Giovambattista, R., Piscini, A. & Cinti, F. R. 2010. Normal faults and thrusts reactivated by deep fluids: The 6 April 2009 Mw 6.3 L'Aquila earthquake, central Italy. *Journal of Geophysical Research*, **115**, B06315, doi: 10.1029/2009JB007190

Doglioni, C., Barba, S., Carminati, E. & Riguzzi, F. 2011. Role of the brittle–ductile transition on fault activation. *Physics of the Earth and Planetary* Interiors, **184** (3-4), 160-171.

Doglioni, C., Carminati, E., Petricca, P. & Riguzzi, F. 2015. Normal fault earthquakes or graviquakes. *Scientific Reports*, **5**, 12110.

Ekström, G., Morelli, A., Boschi, E. & Dziewonski, A. M. 1998. Moment tensor analysis of the central Italy earthquake sequence of September–October 1997. *Geophysical Research Letters*, **25**, 1971-1974.

EMERGEO Working Group 2010. Evidence for surface rupture associated with the Mw 6.3 L'Aquila earthquake sequence of April 2009 (central Italy). *Terra Nova*, **22**, 43-51.

Falcucci, E., Gori, S., Peronace, E., Fubelli, G., Moro, M., Saroli, M., Giaccio, B., Messina, P., Naso, G., Scardia, G., Sposato, A., Voltaggio, M., Galli, P. & Galadini, F. 2009. The Paganica fault and surface coseismic ruptures caused by the 6 April 2009 earthquake (L'Aquila, central Italy). *Seismological Research Letters*, **80**, 940-950.

Farr, T. G., & Kobrick, M. 2000. Shuttle Radar Topography Mission produces a wealth of data. *Eos, Transactions American Geophysical Union*, **81**(48), 583-585.

Farr, T. G., Rosen, P. A., Caro, E., Crippen, R., Duren, R., Hensley, S., Kobrick, M., Paller, M., Rodriguez, E., Roth, L., Seal, D., Shaffer, S., Shimada, J., Umland, J., Werner, M., Oskin, M., Douglas Burbank, D., & Alsdorf, D. 2007. The shuttle radar topography mission. *Reviews of Geophysics*, **45**, RG2004, doi:10.1029/2005RG000183 (also available online at http://www2.jpl.nasa.gov/srtm/SRTM_paper.pdf)

Ferretti, A., Fumagalli, A., Novali, F., Prati, C., Rocca, F. & Rucci, A. 2011. A new algorithm for processing interferometric data-stacks: SqueeSAR. *IEEE Transactions on Geoscience and Remote Sensing*, **49**, 3460-3470.

Ferretti, A., Prati, C. & Rocca, F. 2000. Nonlinear subsidence rate estimation using permanent scatterers in differential SAR interferometry. *IEEE Transactions on Geoscience and Remote Sensing*, **38**, 2202-2212.

Ferretti, A., Prati, C. & Rocca, F. 2001. Permanent Scatters in SAR interferometry. *IEEE Transactions on Geoscience and Remote Sensing*, **39**, 8−20.

Ferretti, A., Savio, G., Barzaghi, R., Borghi, A., Musazzi, S., Novali, F., Prati, C. & Rocca, F. 2007. Submillimeter accuracy of InSAR time series: Experimental validation. *IEEE Transactions on Geoscience and Remote Sensing*, **45** (5), 1142-1153.

Galli, P., Giaccio, B. & Messina, P. 2010. The 2009 central Italy earthquake seen through 0.5 Myr-long tectonic history of the L'Aquila faults system. *Quaternary Science Reviews*, **29**, 3768–3789.

Galli, P., Giaccio, B., Messina, P. & Peronace, E. 2011. Paleoseismology of the L'Aquila faults (central Italy, 2009 Mw 6.3 earthquake). Clues on active fault linkage. *Geophysical Journal International*, **187**, 1119-1134, doi: 10.1111/j.1365-246X.2011.05233.x

Gualandi, A., Serpelloni, E. & Belardinelli, M.E. 2014. Space–time evolution of crustal deformation related to the Mw 6.3, 2009 L'Aquila earthquake (central Italy) from principal component analysis inversion of GPS position time-series. *Geophysical Journal International*, **197**, 174-191.

Hanseen, R.F. 2001. Radar interferometry: data interpretation and error analysis (Kluwer Academic Publishers, Dordrecht).

Hantschel, T., and Kauerauf, A.I. 2009. Fluid Analysis. In Fundamentals of Basin and Petroleum Systems Modeling, 199-245 (Springer, Berlin, Heidelberg).

Hippolyte, J.C., Angelier, J. & Roure, F.B. 1994. A major geodynamic change revealed by Quaternary stress patterns in the Southern Apennines (Italy). *Tectonophysics*, **230** (3-4), 199-210.

Hooper, A., Zebker, H., Segall, P. & Kampes, B. 2004. A new method for measuring deformation on volcanoes and other natural terrains using InSAR persistent scatterers. *Geophysical Research Letters*, **31** (23).

Istituto Nazionale di Geofisica e Vulcanologia - INGV database. http://cnt.rm.ingv.it/ Accessed date: 12 July 2019

Italiano, F., Martinelli, G. & Rizzo, A. 2004. Geochemical evidence of seismogenic-induced anomalies in the dissolved gases of thermal waters. A case study of Umbria (Central Apennines, Italy) both during and after the 1997-1998 seismic swarm. *Geochemistry, Geophysics, Geosystems*, **5**, doi: 10.1029/2004GC000720

Jin, L. & Funning, G. J. 2017. Testing the inference of creep on the northern Rodgers Creek fault, California, using ascending and descending persistent scatterer InSAR data. *Journal of Geophysical Research: Solid Earth*, **122** (3), 2373-2389. doi:10.1002/2016JB013535

Jolivet, R., Lasserre, C., Doin, M. P., Guillaso, S., Peltzer, G., Dailu, R., Sun, J. & Xu, X. 2012. Shallow creep on the Haiyuan fault (Gansu, China) revealed by SAR interferometry. *Journal of Geophysical Research: Solid Earth*, **117**, B06401. https://doi.org/10.1029/2011JB008732

Lanari, R., Casu, F., Manzo, M., Zeni, G., Berardino, P., Manunta, M. & Pepe, A. 2007. An Overview of the Small BAseline Subset Algorithm: A DInSAR Technique for Surface Deformation Analysis. In Deformation and Gravity Change: Indicators of Isostasy, Tectonics, Volcanism, and Climate Change (eds Wolf, D. & Fernández, J.), 637-661 (Birkhäuser Verlag,).

Lanari, R., Berardino, P., Bonano, M., Casu, F., Manconi, A., Manunta, M., Manzo, M., Pepe, A., Pepe, S., Sansosti, E., Solaro, G., Tizzani, P. & Zeni, G. 2010. Surface displacements associated with the L'Aquila 2009 Mw 6.3 earthquake (central Italy): New

evidence from SBAS-DInSAR time series analysis. *Geophysical Research Letters*, **37**, L20309.

Lavecchia, G., Castaldo, R., De Nardis, R., De Novellis, V., Ferrarini, F., Pepe, S., Brozzetti, F., Solaro, G., Cirillo, D., Bonano, M., Boncio, P., Casu, F., De Luca, C., Lanari, R., Manunta, M., Manzo, M., Pepe, A., Zinno, I. & Tizzani, P. 2016. Ground deformation and source geometry of the 24 August 2016 Amatrice earthquake (Central Italy) investigated through analytical and numerical modeling of DInSAR measurements and structural-geological data. *Geophysical Research Letters*, **43** (24).

Lombardi, A.M., Cocco, M. & Marzocchi, W. 2010. On the increase of background seismicity rate during the 1997–1998 Umbria-Marche, Central Italy, sequence: apparent variation or fluid-driven triggering? *Bulletin of the Seismological Society of America*, **100**, 1138–1152.

Lucente, F.P., De Gori, P., Margheriti, L., Piccinini, D., Di Bona, M., Chiarabba, C. & Piana Agostinetti, N. 2010. Temporal variation of seismic velocity and anisotropy before the 2009 Mw 6.3 L'Aquila earthquake, Italy. *Geology*, **38**, 1015-1018, doi: 10.1130/G31463.1

Lündgren, P., Casu, F., Manzo, M., Pepe, A., Berardino, P., Sansosti, E. & Lanari, R. 2004. Gravity and magma induced spreading of Mount Etna volcano revealed by satellite radar interferometry. *Geophysical Research Letters*, **31**, L04602.

Luo, S., Fu, L., Zhu, S., He, Q., Wan, W. & Yang, B. 2013. Processes of the displacement field change of the 2009 April 6 M W 6.3 L'Aquila earthquake using persistent scatterer and small baseline methods. *Earthquake Science*, **26**(5), 293-299, DOI 10.1007/s11589-013-0028-x

Manzo, M., Ricciardi, G.P., Casua, F., Ventura, G., Zeni, G., Borgström, S., Berardino, P., Del Gaudio, C. & Lanari, R. 2006. Surface deformation analysis in the Ischia Island (Italy)

based on spaceborne radar interferometry. *Journal of Volcanology and Geothermal Research,* **151**, 399-416.

Miller, S.A., Collettini, C., Chiaraluce, L., Cocco, M., Barchi, M. & Kaus, B.J. 2004. Aftershocks driven by a high-pressure CO_2 source at depth. *Nature,* **427**, 724–727.

Moro, M., Saroli, M., Stramondo, S., Bignami, C., Albano, M., Falcucci, E., Gori, S., Doglioni, C., Polcari, M., Tallini, M., Macerola, L., Novali, F., Costantini, M., Malvarosa, F. & Wegmüller, U. 2017. New insights into earthquake precursors from InSAR. *Scientific Reports,* **7**, 12035.

Papanikolaou, I.D., Foumelis, M., Parcharidis, I., Lekkas, E.L. & Fountoulis, I.G. 2010. Deformation pattern of the 6 and 7 April 2009, M_W=6.3 and M_W=5.6 earthquakes in L'Aquila (Central Italy) revealed by ground and space based observations. *Natural Hazards and Earth System Sciences*, **10** (1), 73.

Pepe, A., Solaro, G., Calò, F. & Dema, C. 2016. A Minimum Acceleration Approach for the Retrieval of Multi-Platform InSAR Deformation Time-Series. *IEEE Journal of Selected Topics in Applied Earth Observations and Remote Sensing*, **9**, 3883–3898.

Pérez-Peña, J.V., Al-Awabdeh, M., Azañón, J.M., Galve, J.P., Booth-Rea, G. & Notti, D. 2017. SwathProfiler and NProfiler: Two new ArcGIS Add-ins for the automatic extraction of swath and normalized river profiles. *Computer and Geoscience*, **104**, 135-150.

Petricca, P., Barba, S., Carminati, E., Doglioni, C. & Riguzzi, F. 2015. Graviquakes in Italy. *Tectonophysics*, **656**, 202-214.

Picozzi, M., Bindi, D., Zollo, A., Festa, G. & Spallarossa, D. 2019. Detecting long-lasting transients of earthquake activity on a fault system by monitoring apparent stress, ground motion and clustering. *Scientific Reports,* **9,** 16268. https://doi.org/10.1038/s41598-019-52756-8.

Pierantoni, P. P., Centamore, E. & Costa, M. 2017. Geological and seismologic data review of the 2009 L'Aquila seismic sequence (Central Apennines, Italy): deep-seated seismogenic structures and seismic hazard. *Italian Journal of Engineering Geology and Environment*, **17**(2), 5-40.

Pondrelli, S., Salimbeni, S., Morelli, A., Ekström, G., Olivieri, M. & Boschi, E. 2010. Seismic moment tensors of the April 2009, L'Aquila (Central Italy), earthquake sequence. *Geophysical Journal International*, **180**, 238–242.

Quattrocchi, F., Galli, G., Gasparini, A., Magno, L., Pizzino, L. & Voltattorni, N. 2011. Very slightly anomalous leakage of CO_2, CH_4 and radon along the main activated faults of the strong L'Aquila earthquake (Magnitude 6.3, Italy). Implications for risk assessment monitoring tools & public acceptance of CO2 and CH4 underground storage. *Energy Procedia*, **4**, 4067-4075.

Revil, A. & Cathles III, L.M. 2002. Fluid transport by solitary waves along growing faults: A field example from the South Eugene Island Basin, Gulf of Mexico. *Earth and Planetary Science Letters*, **202**, 321-335.

Rossi, G., Zuliani, D. & Fabris, P. 2016. Long-term GNSS measurements from the northern Adria microplate reveal fault-induced fluid mobilization. *Tectonophysics*, **690**, 142-159.

Samsonov, S. & d'Oreye, N. 2012. Multidimensional time-series analysis of ground deformation from multiple InSAR data sets applied to Virunga Volcanic Province. *Geophysical Journal International*, **191**, 1095–1108.

Santo, A., Ascione, A., Di Crescenzo, G., Miccadei, E., Piacentini, T. & Valente, E. 2014. Tectonic-geomorphological map of the middle Aterno River valley (Abruzzo, Central Italy). *Journal of Maps*, **10**, 365-378, doi: 10.1080/17445647.2013.867545.

Savage, M.K. 2010. The role of fluids in earthquake generation in the 2009 Mw 6.3 L'Aquila, Italy, earthquake and its foreshocks. *Geology*, **38**(11), 1055–1056.

Scognamiglio, L., Tinti, E., Michelini, A., Dreger, D.S., Cirella, A., Cocco, M., Mazza, S. & Piatanesi, A. 2010. Fast determination of moment tensors and rupture history: What has been learned from the 6 April 2009 L'Aquila earthquake sequence. *Seismological Research Letters*, **81**, 892–906, doi: 10.1785/gssrl.81.6.892.

Silverii, F., D'Agostino, N., Borsa, A. A., Calcaterra, S., Gambino, P., Giuliani, R. & Mattone, M. 2019. Transient crustal deformation from karst aquifers hydrology in the Apennines (Italy). *Earth and Planetary Science Letters*, **506**, 23-37.

Stemberk, J., Dal Moro, G., Stemberk, J., Blahůt, J., Coubal, M., Košťák, B., Zambrano, M. & Tondi, E. 2019. Strain monitoring of active faults in the central Apennines (Italy) during the period 2002–2017. *Tectonophysics*, **750**, 22-35.

Tarquini, S., Favalli, M., Doumaz, F., Fornaciai, A. & Nannipieri, L. 2012. Release of a 10-m-resolution DEM for the Italian territory: Comparison with global-coverage DEMs and anaglyph-mode exploration via the web. *Computer and Geoscience*, **38**, 168-170, doi: 10.1016/j.cageo.2011.04.018

Terakawa, T., Zoporowski, A., Galvan, B. & Miller, S. A. 2010. High-pressure fluid at hypocentral depths in the L'Aquila region inferred from earthquake focal mechanisms. *Geology*, **38** (11), 995-998.

Tofani, V., Segoni, S., Agostini, A., Catani, F. & Casagli, N. 2013. Technical Note: Use of remote sensing for landslide studies in Europe. *Natural Hazards and Earth System Sciences*, **13**, 299-309.

Valoroso, L., Chiaraluce, L., Piccinini, D., Di Stefano, R., Schaff, D. & Waldhauser, F. 2013. Radiography of a normal fault system by 64,000 high-precision earthquake locations: The 2009 L'Aquila (central Italy) case study. *Journal of Geophysical Research: Solid Earth*, **118**, 1156-1176, doi: 10.1002/jgrb.50130

Valente, E., Buscher, J. T., Jourdan, F., Petrosino, P., Reddy, S. M., Tavani, S., Corradetti, A. & Ascione, A. 2019. Constraining mountain front tectonic activity in extensional setting from geomorphology and Quaternary stratigraphy: A case study from the Matese ridge, southern Apennines. *Quaternary Science Reviews*, **219**, 47-67. https://doi.org/10.1016/j.quascirev.2019.07.001.

ViDEPI Project 2010. Ministero dello Sviluppo Economico (UNMIG), Assomineraria http://unmig.sviluppoeconomico.gov.it/videpi/videpi.asp.

Vilardo, G., Ventura, G., Terranova, C., Matano, F. & Nardò, S. 2009. Ground deformation due to tectonic, hydrothermal, gravity, hydrogeological, and anthropic processes in the Campania Region (Southern Italy) from Permanent Scatterers Synthetic Aperture Radar Interferometry. *Remote Sensing of Environment*, **113**, 197-212.

Villani, F., Civico, R., Pucci, S., Pizzimenti, L., Nappi, R., De Martini, P.M. & the Open EMERGEO Working Group 2018. A database of the coseismic effects following the 30 October 2016 Norcia earthquake in Central Italy. *Scientific Data*, **5**, 180049.

Walters, R.J., Elliott, J.R., D'Agostino, N., England, P.C., Hunstad, I., Jackson, J.A., Parsons, B., Phillips, R.J. & Roberts, G. 2009. The 2009 L'Aquila earthquake (central Italy): A source mechanism and implications for seismic hazard. *Geophysical Research Letters*, **36**, L17312, doi: 10.1029/2009GL039337

Wiggins, C. & Spiegelman, M. 1995. Magma migration and magmatic solitary waves in 3D. *Geophysical Research Letters*, **22** (10), 1289-1292.

Wright, T.J., Parsons, B.E. & Lu, Z. 2004. Toward mapping surface deformation in three dimensions using InSAR. *Geophysical Research Letters*, **31**, L01607, doi:10.1029/2003GL018827 (1).

FIGURE CAPTIONS

Fig. 1. Seismicity of the central Apennines in the last decades, and large-scale topographic features of the 2009 L'Aquila earthquake region. (a) Epicentres and magnitudes of the main earthquake sequences occurred in the last decades in the central Apennines (location in upper right inset), after INGV database (http://cnt.rm.ingv.it/), and focal mechanisms of the main shocks of each sequence (Ekström et al., 1998; Chiarabba et al., 2009; INGV database, http://cnt.rm.ingv.it/). Traces of faults activated at the surface with the main shocks of the various sequences (from Cinti et al., 2000; EMERGEO Working Group, 2010; Lavecchia et al., 2016; Villani et al., 2018; Stemberk et al., 2019) are shown, including the Paganica Fault (from Galli et al., 2010), which was activated with the Mw 6.3 2009 L'Aquila main shock. The white rectangle indicates the study area. Location of the San Donato deep well (ViDEPI, 2010) and traces of the swath profile in B and of Transect A of Fig. 2 are also shown. (b) Swath profile across the 2009 L'Aquila earthquake region, imaging difference of mean elevation between the blocks in the NE and SW of the Paganica Fault. (c) Interpreted seismic reflection profile (after Pierantoni et al., 2017) showing the active extensional fault system of the study area (vertical scale is in two-way time, twt; the original seismic profile is line IT 89-01 available from the ViDEPI Project at https://www.videpi.com/videpi/videpi.asp).

Fig. 2. Time series of Envisat PS data along Transect A (location in Fig. 1) showing displacements recorded along the ascending and descending orbits in the entire 2002-2010 analysed time window, and results of the parametric trend analysis for the preseismic interval. Time series linear regression was computed for each PS and the results tested with ANOVA at an alpha level of 0.05 for the time span considered. Transect A is 300 m buffered. (a) PS time series from Envisat ascending orbit. The general time series pattern is sub-

horizontal, meaning no net motion relative to satellite in the entire preseismic period. Following the coseismic collapse, in the postseismic time frame, the general pattern is sub-horizontal. (b) PS time series from Envisat descending orbit. PS motion towards satellite, i.e. positive trend, during the early part of the record (Preseismic Stage 1) is visible and clearly identified by the trend analysis in the first c. 15 km to the west of the Paganica Fault. Note that the segment of Transect A subject to motion towards satellite during Preseismic Stage 1 is subsequently affected by negative displacement (Preseismic Stage 2, from September/October 2008 to February 2009). Coseismic collapse along the 15 km long eastern segment of Transect A is followed by negative motion continuing until June 2010.

Fig. 3. Parametric trend analysis performed on Envisat Permanent Scatterers time series data for the 2009 L'Aquila earthquake preseismic period. The two diagrams show spatial distribution of Envisat PS with indication of PS trend behaviour; the acquisition geometries of the Envisat ascending and descending orbits are shown in the insets. The trace of the Paganica Fault is also shown in the diagrams. Time series linear regression was computed for each PS and the results tested with ANOVA at an alpha level of 0.05 for the time span considered. Blue points indicate positive linear deformation trends; red points indicate significant negative linear deformation trends; yellow points indicate that linear trends are not significant. a: ascending orbit PS data; the analysed time span corresponds to the entire preseismic record (November 2002 to March 2009). b: descending orbit PS data; the analysed period spans from November 2002 to September 2008 (Preseismic Stage 1).

Fig. 4. Verification of the assumptions of the parametric trend analysis. This figure synthesises the results of the Lilliefors (upper diagrams) and Durbin-Watson (lower

diagrams) tests computed to check the assumptions on normality and non-autocorrelation of linear regression residuals of the Envisat PS ascending track (diagrams in the left side) and Envisat PS descending track (diagrams in the right side) time series. Green and red points indicate failure to reject and rejection of the tested null hypothesis at 0.05 alpha level, respectively.

Fig. 5. Non-parametric trend analysis performed on Envisat Permanent Scatterers time series data for the 2009 L'Aquila earthquake preseismic period. Analysed PS data are from the region in which, through the visual analysis of time series of PS from the descending orbit dataset, distinct preseismic displacement patterns have been identified. According to Mann-Kendall test (0.05 alpha level) and Theil-Sen's slope estimation, blue points indicate significant positive linear deformation trends; red points indicate significant negative linear deformation trends; yellow points mark non-significant trends. The trace of the Paganica Fault is also shown. a: ascending orbit PS data; the analysed time span corresponds to the entire preseismic record (November 2002 to March 2009). b: descending orbit PS data; the analysed period spans from November 2002 to September 2008 (Preseismic Stage 1).

Fig. 6. Ground displacement vs. precipitation in the area of the 'L'Aquila S. Elia' meteorological station for the 2000-2010 time interval. The dash-dotted line indicates occurrence of the 6th April 2009 earthquake. Upper diagrams show mean displacement (black line) and 1-σ envelope (shaded area) of PS-InSAR descending (a) and ascending (b) data computed from 200 data points located in the area of the 'L'Aquila S. Elia' meteorological station (Latitude: 42°20'03'', Longitude: 13°25'43''; elevation: 590 m a.s.l.). In the lower diagrams, precipitation data are shown. (c) Monthly rainfall time series (grey

line) of the 'L'Aquila S. Elia' meteorological station; black line indicates moving average smoothing of monthly precipitation. (d) Detrended cumulative rainfall data. The pre-seismic uplift of the hanging wall of the Paganica Fault, clearly outlined by the trend in diagram a, is unrelated with the precipitation trend shown in diagrams (c) and (d).

Fig. 7. Periodogram of the 'L'Aquila S.Elia' meteorological station (Latitude: 42°20'03'', Longitude: 13°25'43'', elevation: 590 m a.s.l.) 2000-2018 time series. The time series consists of 228 monthly precipitation values. Periodogram power peaks correspond to periods of about 6, 12 and 57 months.

Fig. 8. Spatial distribution of pre- to post-seismic ground deformation in the study region. Vertical (up/down) and horizontal (E/W) components of ground deformation in the maps of diagrams a to d are obtained by combination of PS-Envisat data from ascending and descending orbits; diagram e shows mean velocity towards satellite estimated from COSMO-SkyMed PS data obtained by the descending track. Strands of the Paganica Fault system and epicentre of the 6th April 2009 main shock are indicated. Trace of profiles of Fig. 10 and locations of GPS stations INGP and AQUI are also shown. (a) Vertical (left side) and horizontal (right side) components of ground deformation summed up during Preseismic Stage 1; the block in the SW of the PF is affected by E-oriented uplift. (b) Vertical (left) and horizontal (right) components of ground deformation summed up during Preseismic Stage 2; the region in the SW of the PF experienced subsidence with W-oriented component. (c) Vertical component of coseismic displacement, is focused in the PF hanging wall block, though part of the footwall block is also downthrown. (d) Vertical component of early (one year) postseismic ground motions, showing subdued subsidence of the PF hanging wall

block. (e) Late postseismic deformation, showing negative motion of the PF hanging wall block continuing through year 2014.

Fig. 9. 3D view of the coseismic displacement (vertical exaggeration × 18,000), with indication of mean values of estimated positive/negative displacement. The Paganica Fault trace is shown in red.

Fig. 10. Topography vs. profiles of vertical displacement extracted by the maps of Fig. 8, along a transect transverse to the Paganica Fault trace (location in Fig. 8a, b and c). Diagrams show vertical displacement summed up during Stage 1 and Stage 2 of the preseismic period, and in the coseismic stage, respectively. Note change of vertical scale in the lowest diagram. The PF marks the boundary between the blocks that, in Preseismic Stages 1 and 2, experienced reversals of displacement.

Fig. 11. Reconstructed seismic cycle for the Aquila area. (a) During the interseismic stage, aseismic creep along the deep, gently dipping detachment produces fracturing above the detachment fault tip and in the hanging wall of the locked normal fault (red). (b) Further extensional strain leads to fracturing also within the locked fault zone, including the fault core, reducing its sealing capacity. (c) Continued aseismic slip along the detachment fault produces further dilation in the hanging wall of the locked fault. CO_2 pore pressure can no longer sustain the load of the overlying rock volume, which starts subsiding as incipient collapse of fracture porosity occurs. This process is accompanied by rupturing of patches of the previously locked fault, thereby generating small to moderate size earthquakes (foreshocks). (d) The mainshock occurs as catastrophic collapse of fracture porosity takes

place, accompanied by rupturing of the entire seismogenic fault surface. (e) Further hanging-wall subsidence is associated with collapse of the residual fracture porosity and is accompanied by further rupturing of fault patches, generating aftershocks during the early postseismic stage. A multi-year persistence of hanging-wall negative ground motion is associated with afterslip during the late postseismic stage.

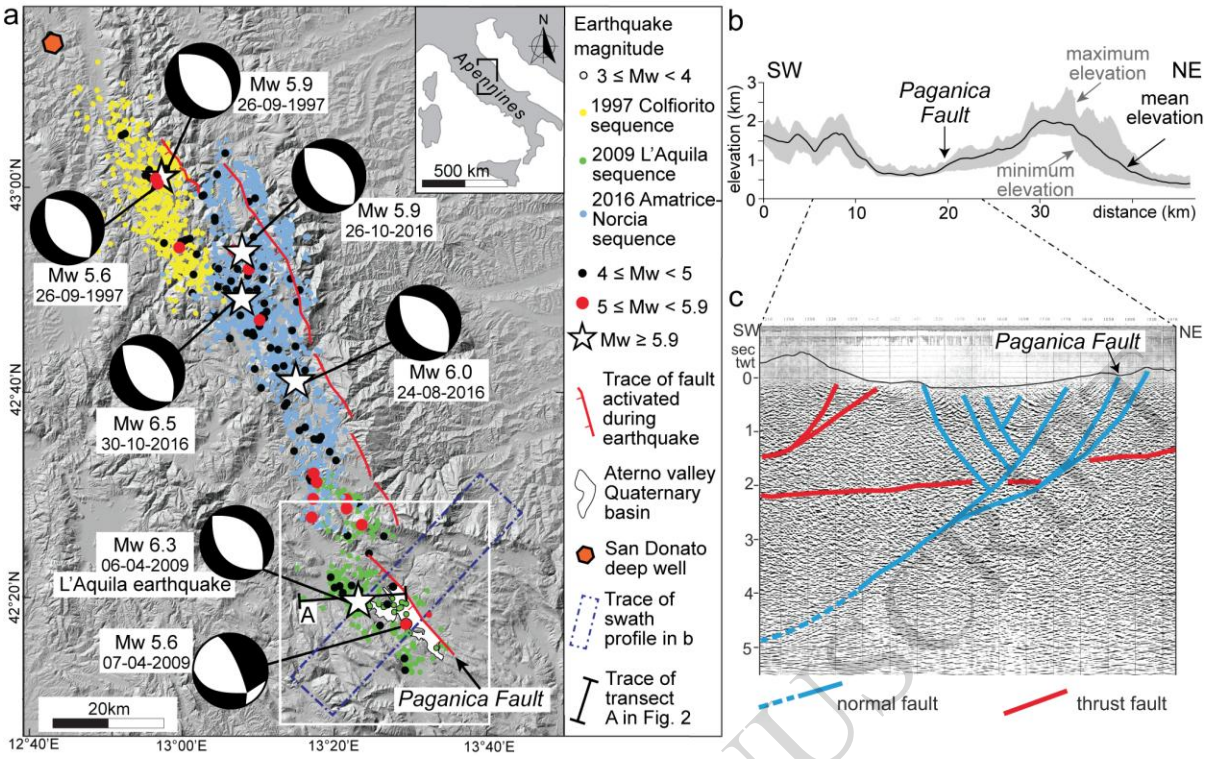

Figure 1

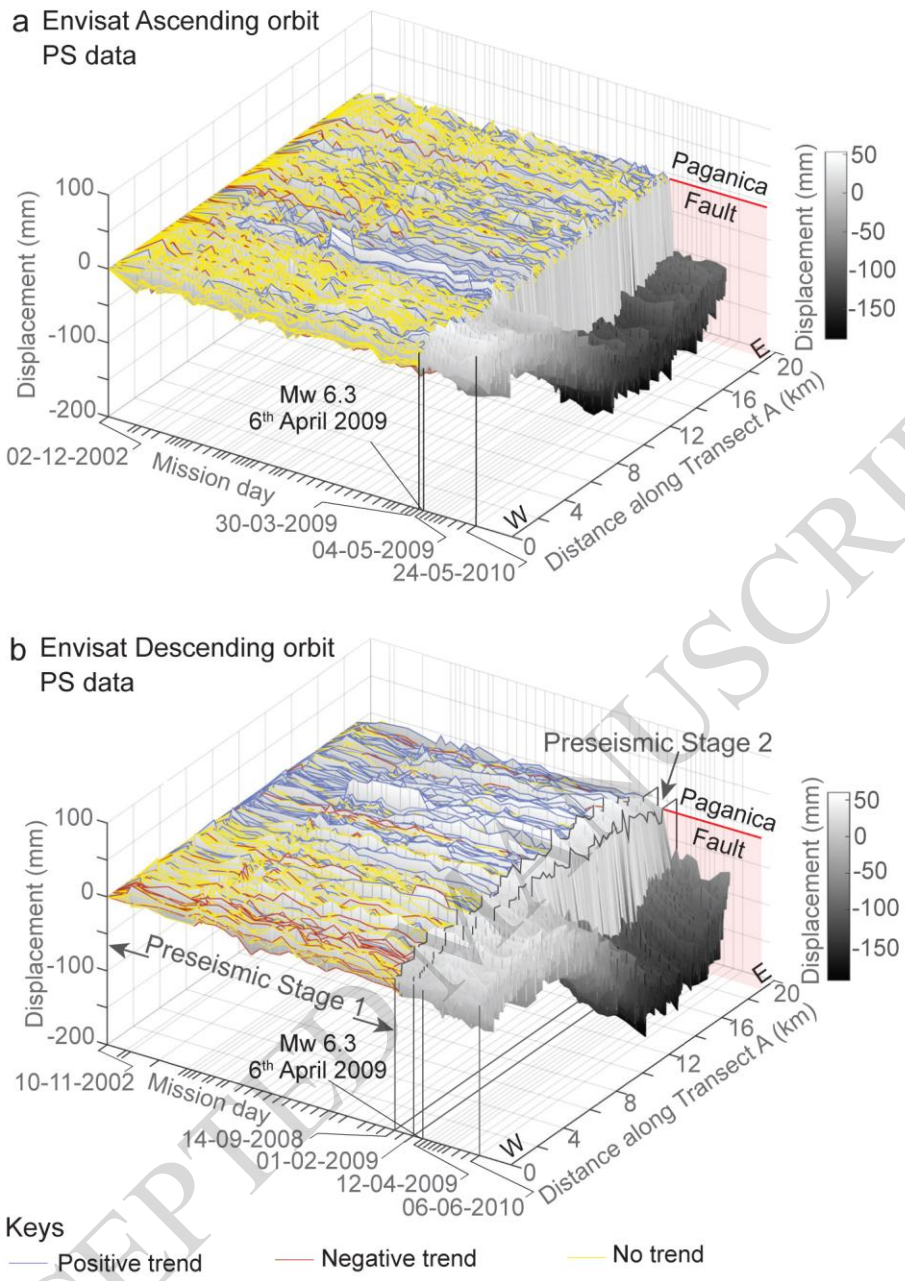

Figure 2

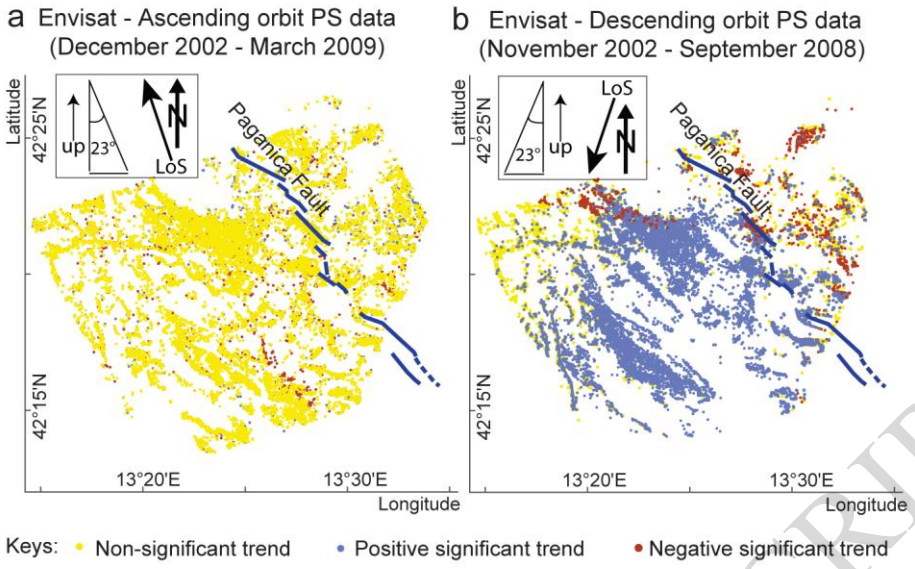

Figure 3

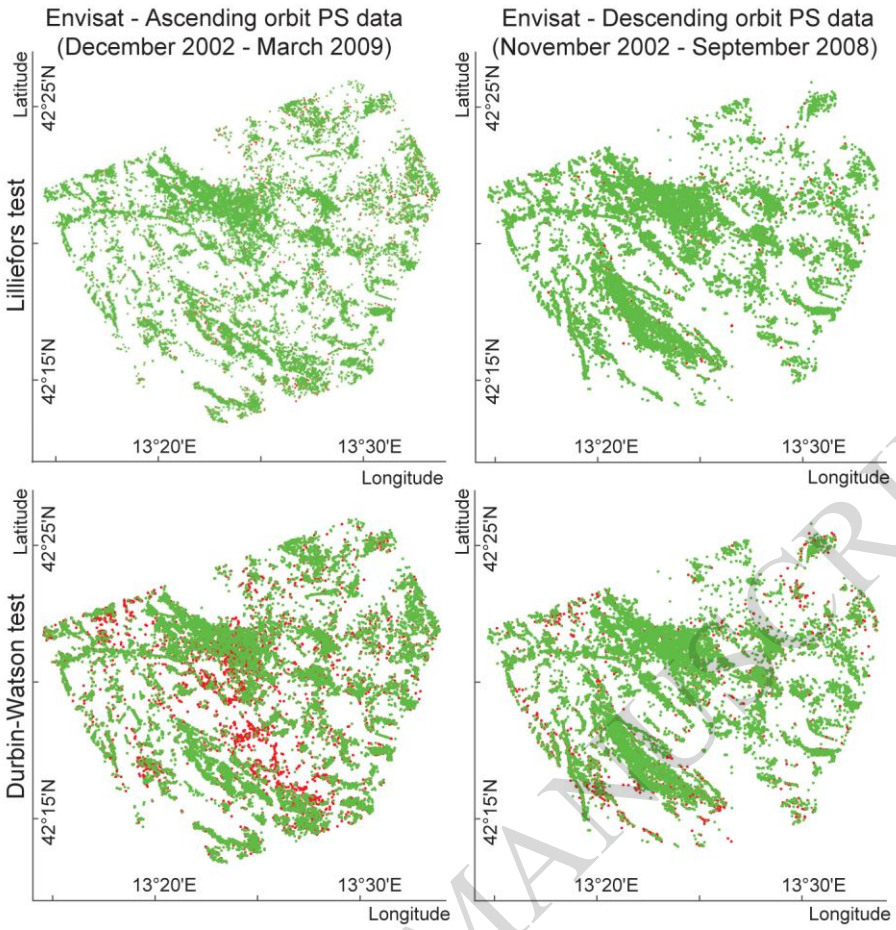

Figure 4

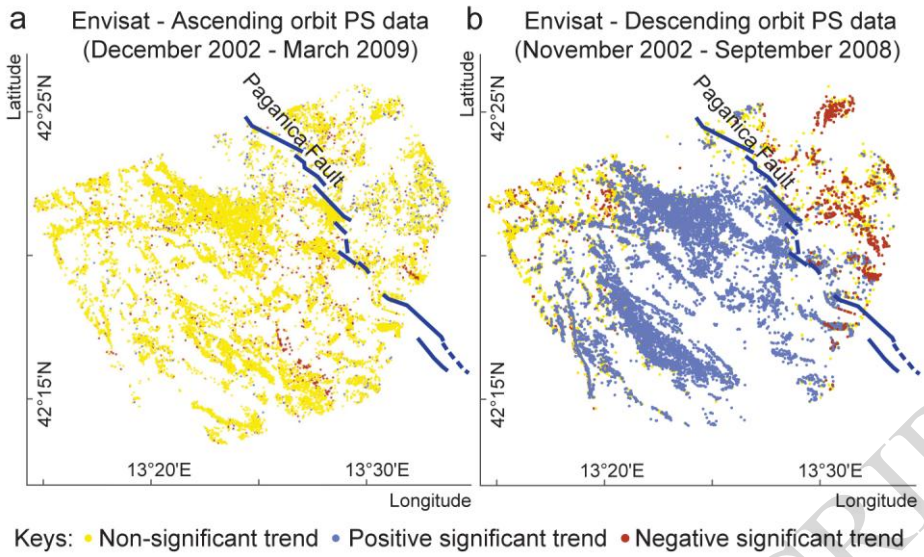

Figure 5

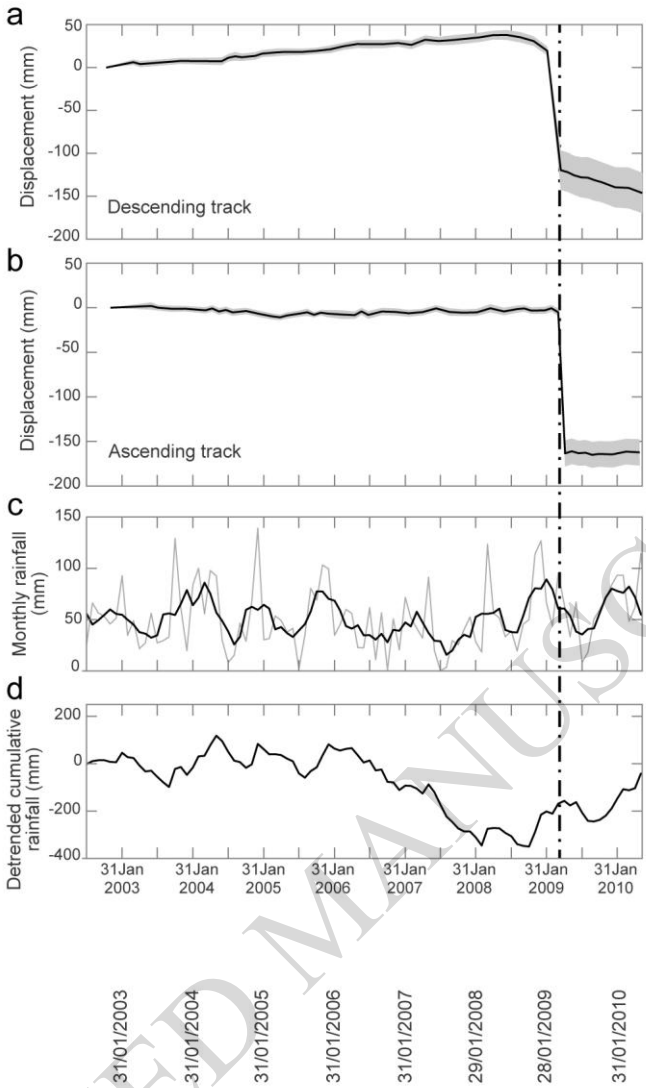

Figure 6

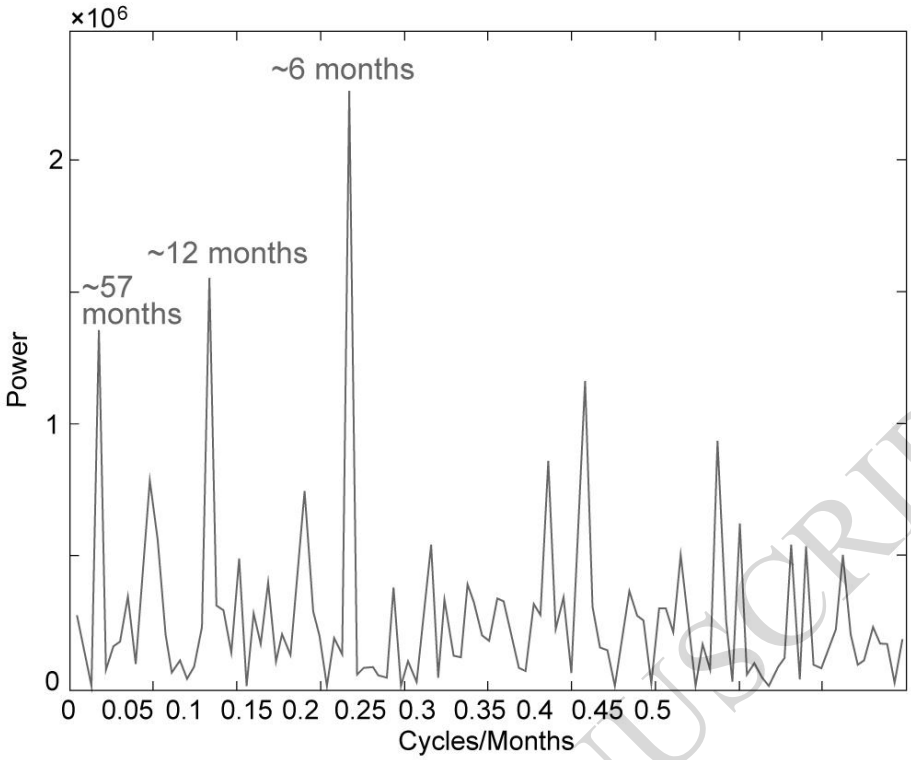

Figure 7

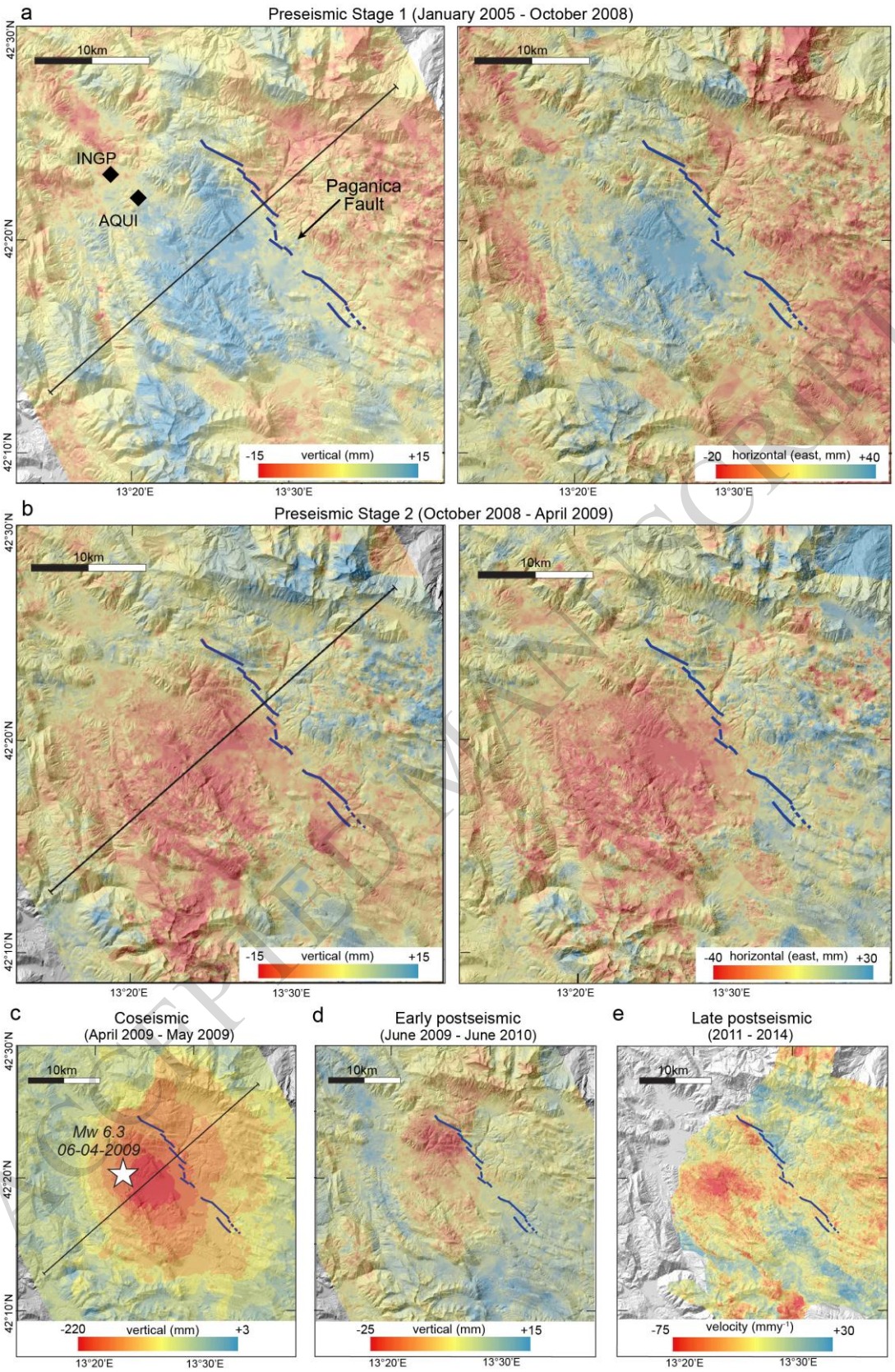

Figure 8

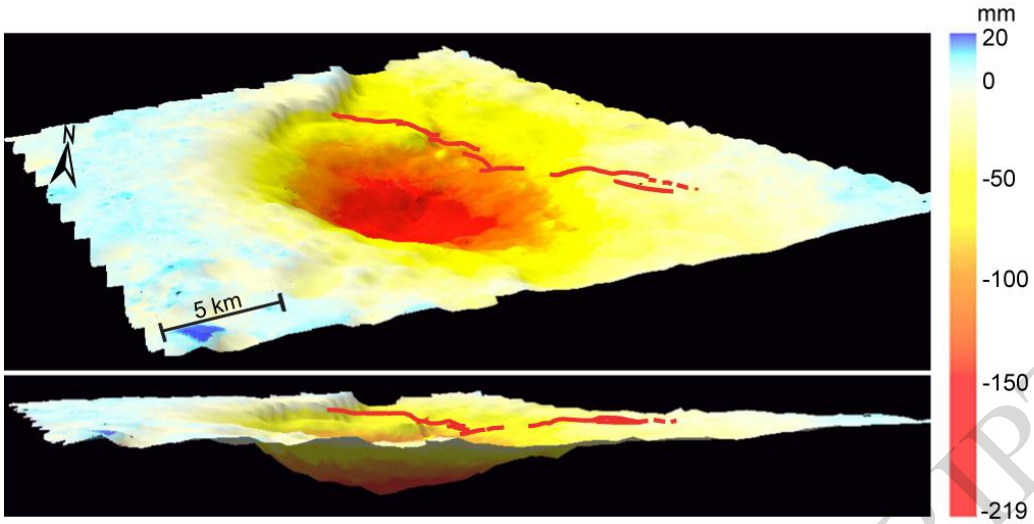

Figure 9

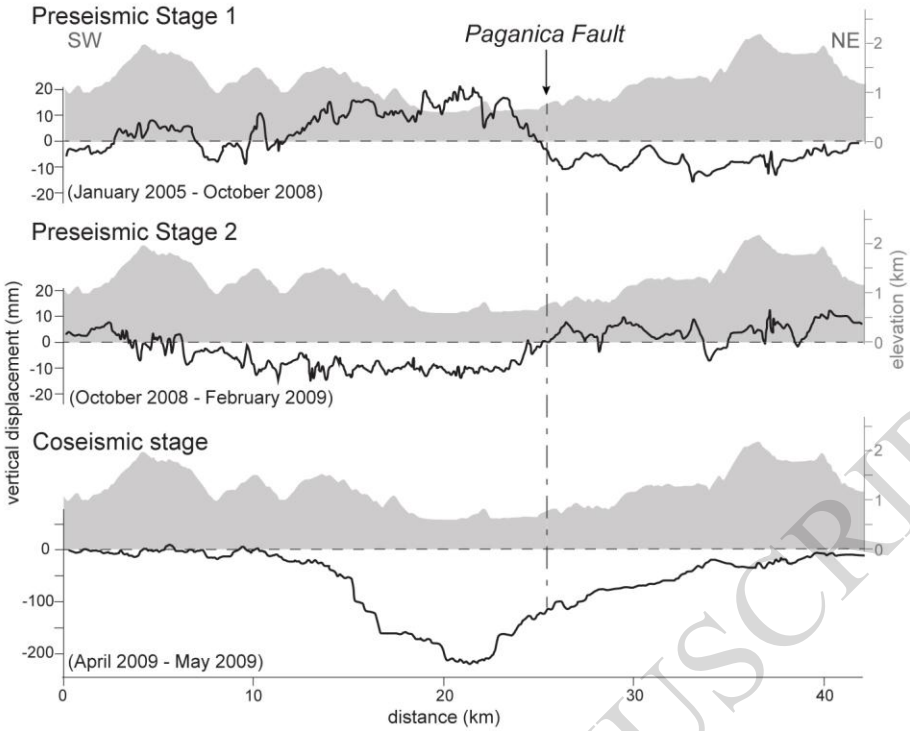

Figure 10

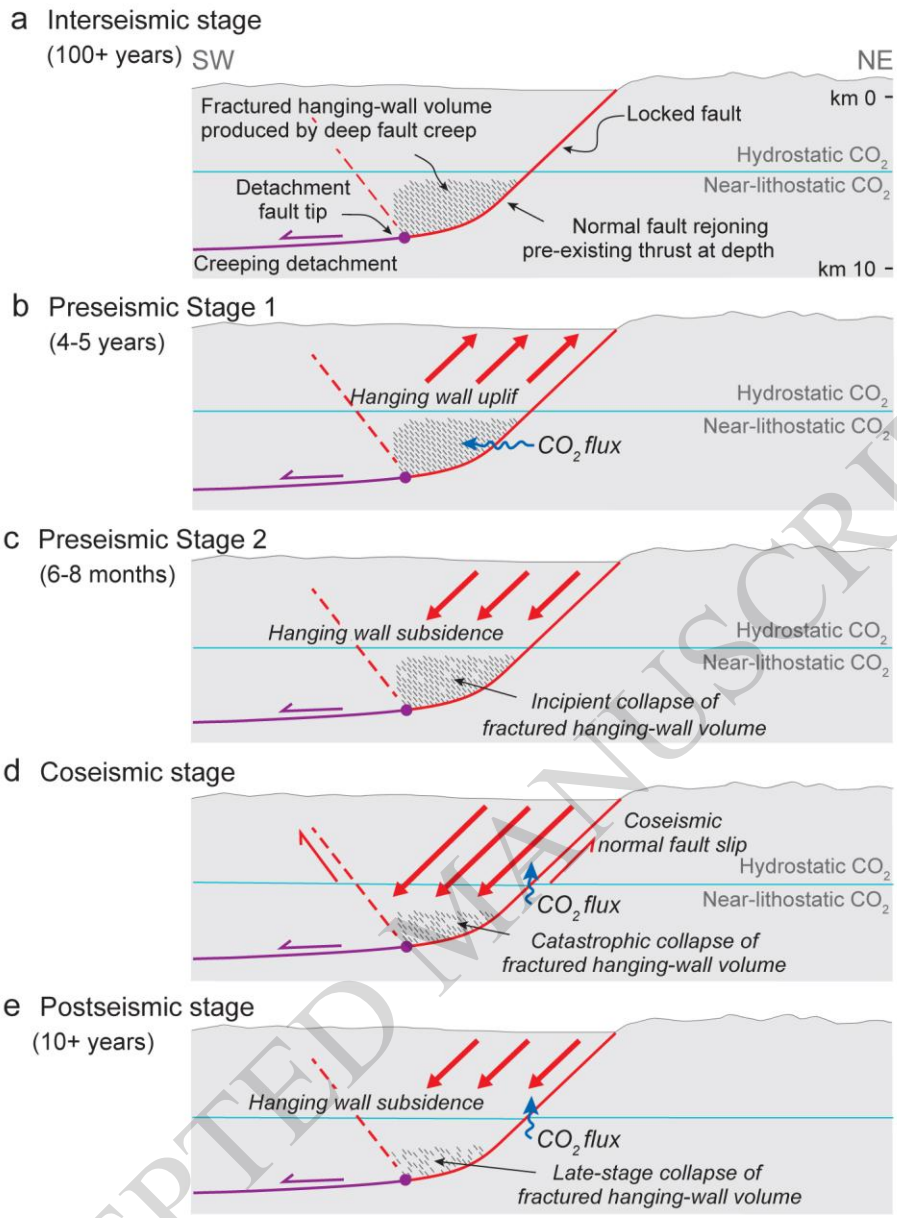

Figure 11

Table 1 – Permanent Scatterer datasets used in this study

Satellite	Orbit	Track/Frame	LoS incidence angle	Number of PS/frame
ERS	Descending	pst_ers_t308_f2751_cl001_l_aquila	23.44	42573
		pst_ers_t308_f2769_cl001_sulmona	23.25	69065
	Ascending	pst_ers_t129_f837_cl002_pineto	23.36	47650
		pst_ers_t129_f837_cl001_celano	23.80	126131
Envisat	Descending	PST2009_ENVISAT_T79_F2748_CL001_AQUILA	22.75	127089
		PST2009_ENVISAT_T308_F2751_CL001_TERAMO	22.71	341759
	Ascending	PST2009_ENVISAT_T401_F840_CL001_AQUILA	22.80	270047
		PST2009_ENVISAT_T129_F837_CL001_CHIETI	22.79	308357
COSMO-SkyMed	Descending	PST2013_CSK_F_74_AQUILA_D_CL001	32.19	1764739